PREFERENTIAL NUCLEATION OF COBALT NANOCLUSTERS ON THE

FACETED RHENIUM (12 $\bar{3}$ 1) SURFACE

By

MERAL REYHAN

A thesis submitted to the

Graduate School-New Brunswick

Rutgers, The State University of New Jersey

in partial fulfillment of the requirements

for the degree of

Master of Science

Graduate Program in Physics

written under the direction of

Professor Ted Madey

and approved by

_____

_____

_____

New Brunswick, New Jersey

October, 2007

ABSTRACT OF THE THESIS

Preferential Nucleation of Cobalt Nanoclusters on the Faceted Rhenium(12 $\bar{3}$ 1) Surface

By MERAL REYHAN

Thesis Director:
Professor Ted Madey

We have studied the preferential nucleation of cobalt nanoclusters on oxidized faceted

rhenium(12 $\bar{3}$ 1) by means of Auger electron spectroscopy (AES), low energy electron

diffraction (LEED), and scanning tunneling microscopy (STM). Preferential nucleation

means that the Co nanoclusters form at specific sites on the substrate. In contrast to

previous nanostructure studies of preferential nanocluster nucleation in metal on metal

experiments, we use a surface that is both oxidized and faceted to form a nanotemplate.

It is shown that for cobalt coverage between 1.6 ML and 3 ML, preferential nucleation of

cobalt nanoclusters occurs on this faceted surface. It is also shown that by varying the

parameters of cobalt coverage, facet width and annealing temperature, the cobalt

nanocluster size can be varied. The cobalt nanocluster system may prove to be a model

system for future studies of different substrates and overlayers more relevant to catalytic

reactions.

Acknowledgement

This work would have been impossible without the support and guidance of Professor Theodore Madey during my studies at Rutgers University. I would like to thank Dr. Madey for giving me the opportunity to work in his group, which was a great experience for me. I would also like to thank Mr. Hao Wang for introducing me to the experimental setup and all its secrets, for his patience and advice. I would like to thank my family for all of their support during my academic career. I would especially like to thank Cassie for letting me accompany her on long walks around the neighborhood.

Table of Contents

Lists of Tables

List of Illustrations

Chapter 1

Introduction

Applications for nanowires are limited only by the imagination. Nanowires are currently being used in electronics, optics, mechanics, catalysis, and sensing technology. These wires are capable of connecting with different kinds of molecules that compose the human body having applications as biological sensors for measuring anything from certain hormone levels in pregnant women to glucose levels in diabetics [6]. Nanowires composed of different materials have different properties, further augmenting their applications. These wires are the building blocks for future nanoscale devices. Due to the rapidly growing interest, new techniques for nanowire creation are necessary.

Currently nanowires are created in a myriad of ways; amongst the most common ways are suspension and synthesis. A suspended nanowire is often produced by chemical etching of a larger wire or showering energetic particles on a larger wire under vacuum conditions. Another popular technique for the creation of suspended nanowires is using a Scanning Tunneling Microscope (STM) on the surface of a metal heated near its melting point. By contacting the tip of the STM on the surface of this metal and then retracting the tip, a nanowire can be drawn from the metal's surface [26].

Another common method for creating nanowires is synthesis. A popular synthesis technique is called the Vapor-Liquid-Solid (VLS) synthesis method.   This method uses a source material such as a feed gas or laser ablated (dissipated by melting) particles. The source is exposed to a catalyst, such as liquid metal nanoclusters, which enters the nanocluster and begins to saturate it. Once the nanocluster is supersaturated,

the source solidifies and grows outward. By controlling the amount of the source that is used, the shape and height of the nanowire can be regulated [9].

Vapor deposition is a technique that is frequently used to create nanowires. Evaporative deposition is a process in which a thin film of metal is deposited onto a substrate by being converted into a vapor, then being transported through a region of low pressure to the substrate's surface, and finally condensing on the substrate forming a film [29].   In the present experiment, this is the primary technique used for delivering atoms to the substrate. Another deposition technique, known as electrochemical deposition is frequently used in the creation of nanowires. A metal surface for deposition is connected to the negative terminal of a voltage source and the metal to be deposited is connected to the positive terminal. The two objects are placed in an electrolyte and when the battery is turned on, a current passes through the electrolyte, which reduces the metal ions to be deposited forming a solid metal on the desired surface [20].

One of the first scientists to grow nanowires was Dr. H. Roeder. In his paper published in 1993, "Building One- and Two-Dimensional Nanostructures by Diffusion-Controlled Aggregation at Surfaces", he was able to aggregate Cu in the $(1\bar{1}0)$ channels of a Pd(110) substrate. From Roeder's paper, many other scientists were inspired to further the study of nanostructures. The following picture is from Roeder's paper illustrating the Cu chains on Pd(110) [23].

Figure 1. The copper nanochains [24] were aggregated on the Pd(110) substrate by controlled

While it looks like only certain channels have Cu chains within them, this is not true. Since the image is displayed on such a limited scale, it is difficult to see that all the channels have Cu chains in them [23].

The mechanism for the growth of the chains is thought to be caused by the collision of two diffusing Cu atoms, which form a relatively immobile nucleus. Once the Cu nucleus is trapped in a channel, more diffusing Cu atoms congregate around this single nucleus. This in turn leads to Cu atom chains of variable lengths. By varying the deposition temperature, they were able to change the average lengths of the Cu chains. For temperatures of 300 K, the average Cu chains are hundreds of Angstroms (Å) long. For temperatures less than 300 K, a Cu chain's average length decreased to tens of atoms in length. For temperatures greater than 300 K, islands of Cu formed. The primary measuring technique used in this paper was scanning tunneling microscopy [23].

An informative paper on the topic of nanowire growth was written by Gambardella et al., who studied Co deposited onto a stepped Pt(997) surface. In this paper, thermal energy atomic scattering (of helium atoms), TEAS, is utilized. Due to the low incident energies used (10-300 meV), the incident helium atoms probe the topmost surface layer of the substrate. The topmost layers of a crystalline material diffract the helium atoms and the periodic arrangement of the atoms in crystals determines the direction of the diffracted helium atoms. TEAS leads to diffraction patterns with maxima at the Bragg positions, which correspond to the reciprocal super lattice of the substrate. The diffraction peak intensities depend only on the topmost layer of atoms. The other experimental technique used was scanning tunneling microscopy. Gambardella et al.

were able to show periodic arrays formed between temperatures of 250 to 300 K. The

cobalt formed nanowires along the step-edges. The following picture is an atomically

resolved STM image of Co wires on Pt(997) [7].
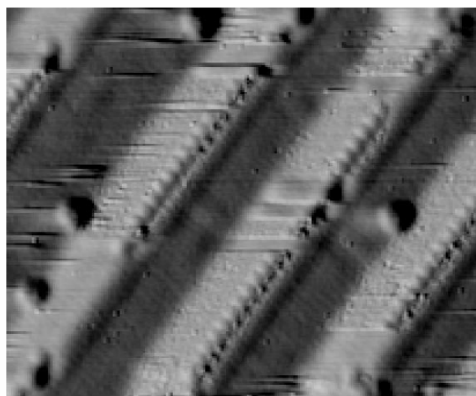
Figure 2. After a dz/dx (x-slope) background subtraction, it is clear from this atomically resolved STM image that after depositing 0.07 ML of Co at 250 K, Co chains form at the step edges of the Pt surface [7].

Another paper by Gambardella et al., deals with the ferromagnetic properties of

one dimensional monoatomic chains. The main experimental technique used to classify

the surface consisted mainly of X-ray magnetic circular dichroism, XMCD. The

amplitude of the dichroic signal is a measurement of the magnetization of the nanowire.

The group compared the magnetization measured with a calculated formula for

magnetization to determine the number of atoms in the nanowire. The group showed that

short and long range ferromagnetic order existed for one dimensional cobalt chains on a

platinum substrate. It was also shown that the long range ferromagnetic order occurs due

to a threshold temperature (T < 15 K) and an anisotropic barrier. The typical length of a

continuous cobalt nanowire is approximately 80 atoms at a temperature of 45K [8].
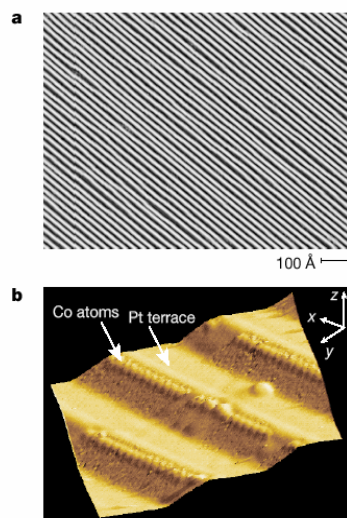
Figure 3a. The original stepped surface before Co deposition. Figure 3b. Co monatomic chains decorate the step edges of the Pt surface after 0.13 ML of Co is evaporated onto the substrate held at 260K [8].

We decided to try a novel approach to the fabrication of nanowires, that is, to nucleate metallic nanowires on a templated surface. Most previous studies were for metals on metal surfaces. Our approach is different because we are using a nanotemplated substrate that is covered in oxygen, approximating a potentially insulating oxide. In this paper, a faceted $Re(12\bar{3}1)$ surface is used as a template for the growth of cobalt nanowires. We wanted to see if vapor-deposited Co would grow randomly or if it would nucleate at specific sites. Through the use of measurements from AES (Auger Electron Spectroscopy), LEED (Low Energy Electron Diffraction), and STM (Scanning Tunneling Microscopy), the study of nanowire nucleation on a faceted oxygen terminated surface was accomplished. While the original goal of this thesis was to discover whether nanowires would nucleate on this structured surface, the ultimate results show that, under certain experimental conditions, the Re template does not produce nanowires, but instead, preferential nucleation of rows of nanoclusters is observed.

Figure 4 shows a schematic diagram of the facets which form on Re($12\bar{3}1$), after the deposition of oxygen and heating in vacuum. As will be discussed in more detail below, long ridges containing ($01\bar{1}0$) and ($11\bar{2}1$) oriented facets cover the surface. When Co is deposited and the surface is annealed, we do not see nanowires of Co that nucleate at sites in the bottoms of the troughs (Figure 4 b). However, we do see nanoclusters of Co which preferentially nucleate in the troughs of the facets (Figure 4 c).

($01\bar{1}0$)

($1\bar{1}\bar{2}1$)

a)

Atomic Structure of (01-10)

Atomic Structure of (11-21)

b)

c)
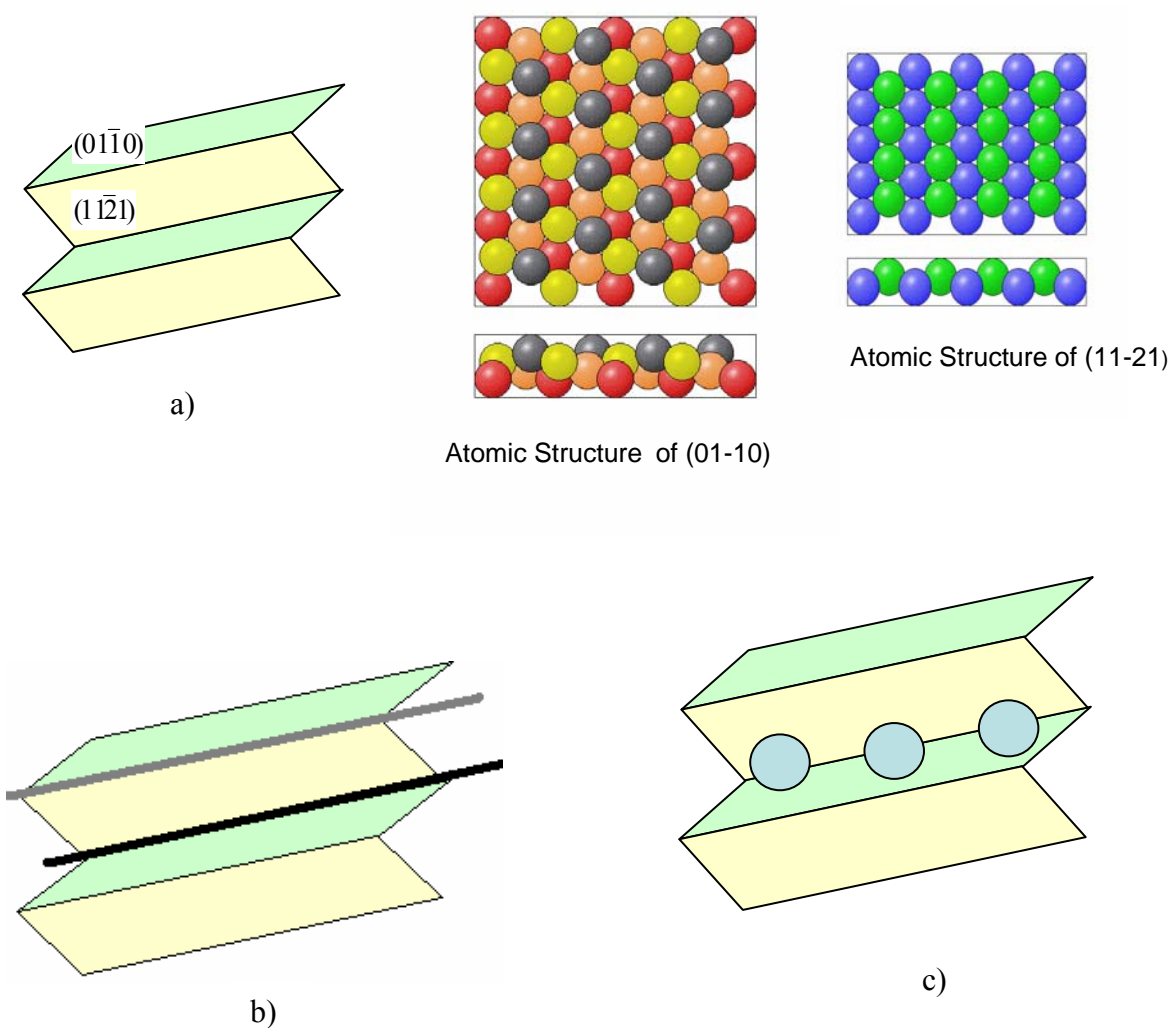
Figure 4. Illustration a) shows the faceted Re(12-31) surface and the atomic structure of the two facets. Illustration b) depicts possible nucleation sites for the Co nanowires with black and gray 'wires'. Illustration c) shows the preferential nucleation site of the Co nanoclusters.

Chapter 2

Growth and Preferential Nucleation

Extensive studies have been performed to show that in general there are three distinct growth modes for films on metal surfaces, each named after the discovering scientists, Frank-Van der Merwe (FV) growth, Volmer-Webwer (VW) growth, and Stranski-Kranstanov (SK) growth [32]. These modes are usually used for describing growth due to vapor deposition. FV growth is also known as layer-by-layer growth because the deposited atoms cover the entire surface, forming single atomic layers upon layers as they grow. During the first layer of deposition, the overlayer atoms bond more strongly to the substrate than to other overlayer atoms. After the first overlayer is formed, the atoms bond equally to the atoms underneath and other overlayer atoms. For this reason either FV or SK growth can occur. In SK growth, or layer and island growth, layers and islands coexist on the surface. Overlayer strain due to lattice parameter difference differentiates SK from FV growth, forming islands instead of layers. In VW growth, or island growth, the deposited atoms form isolated "three-dimensional crystallites" or islands before covering the entire surface. VW growth occurs because the overlayer atoms find bonding with other overlayer atoms more preferable than bonding with substrate atoms [32].

Using simple analysis, prediction of the three growth modes is possible. If the surface free energy of the substrate vacuum interface is greater than the surface free energy of the overlayer vacuum interface plus the surface free energy of the substrate overlayer interface, then FV layer growth will occur. VW growth will take place if the

surface free energy of the substrate vacuum interface is less than the surface free energy

of the overlayer vacuum interface plus the surface free energy of the substrate overlayer.

If the surface free energy of the substrate vacuum interface is approximately equal to the

surface free energy of the overlayer vacuum interface plus the surface free energy of the

substrate overlayer, then SK growth will occur [32]. Although, these three modes are

thermodynamic equilibrium modes, even away from equilibrium this is a useful

classification.

Frank Van der
Merwe growth

Volmer-Weber
growth

Stranski-Krastanov
growth
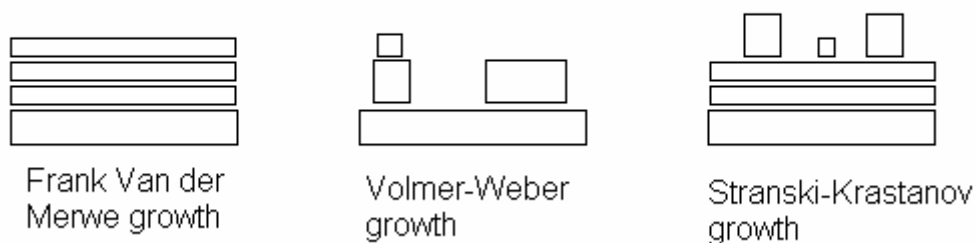
Figure 5. The three different growth modes are illustrated by block models.

The three growth modes occur through a process known as nucleation, where

small stable clusters of two or more atoms, called nuclei, form at different sites on the

surface. As the surface starts to fill with nuclei, they can amalgamate forming larger

nuclei, ultimately covering the surface in one of the three growth modes.   Nucleation is

divided into two categories: homogeneous nucleation and heterogeneous nucleation.

Homogeneous nucleation, Figure 6, is so named because the surface is assumed to be

defect free and nuclei are formed when atoms diffuse, collide, and form clusters at

random sites. In heterogeneous nucleation, the surface is assumed to be irregular; the

irregularities take the form of defects. These defects can be intrinsic like steps, kinks,

and terraces or extrinsic like adatoms, clusters, and advacancies. Preferential nucleation,

a form of heterogeneous nucleation, implies that there are particular sites on the

substrate's surface at which nucleation occurs the most frequently [19].
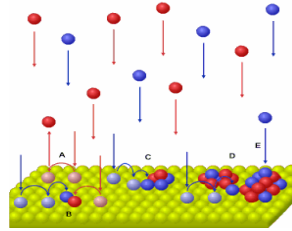
Figure 6. Atoms are deposited and then diffuse on a defect free surface, illustrating homogeneous nucleation [19].

Homogeneous nucleation occurs when atoms diffuse on a surface to form nuclei.

The nuclei are formed after deposited atoms collide and remain stuck together. After

several collisions, the atoms begin to form a cluster. The radius of the cluster is governed

by energetics, which determines when a stable nucleus size is reached. This minimum

radius size, known as the critical cluster size, can be determined by the following formula

for total free energy:

Volume Free Energy   Surface free Energy

$$\Delta G_{(r)} = \frac{4}{3}\pi r^3 \Delta G_v + 4\pi r^2 \gamma_{SL} \quad .$$

Taking the derivative with respect to r and setting it to zero, i.e., the maxima in Figure 7,

and then solving for r gives the formula for critical cluster size:

.
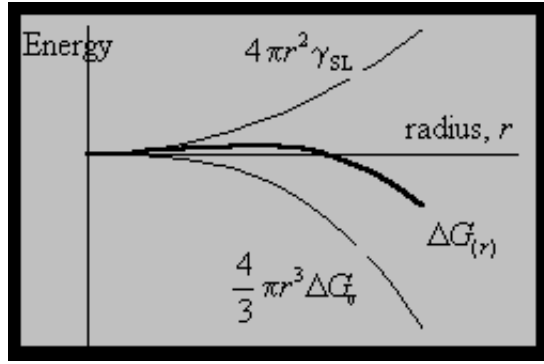
$$r^* = \frac{-2\gamma_{SL}}{\Delta G_v}$$

Figure 7. Critical nucleus size can be determined from this energy versus radius graph.

If the cluster radius, r, is greater than the critical cluster size, r*, then the nucleus is stable and if it is less than the critical cluster size, r*, the nucleus is unstable. The critical cluster size is a key factor in homogeneous nucleation [19]. For many systems, the critical cluster size is one or two atoms.

Adopting a model where homogeneous nucleation occurs in the first layer and adatoms desorb slowly, the saturation density (nuclei/unit area), N, of nuclei can be calculated. The saturation density is then reached when the diffusing atoms find an existing nucleus before finding another diffusing atom with which forming a new nucleus is possible. The formula used to calculate N is:

$$N \sim (F/D)^{(x)} \exp\{E_i/((i+2)*kT)\},$$

where F is the vapor deposition flux (atoms/area/second), D is the diffusion coefficient, i is the number of atoms in the critical nucleus, E_i is the critical nucleus binding energy, and exponent x=i/(i+2). From this formula, it is clear that the saturation density increases with vapor flux and binding energy and decreases with increasing diffusion coefficient and temperature.

The Ehrlich-Schwoebel barrier controls heterogeneous nucleation. Once atoms are deposited on the heterogeneous substrate surface, they begin to diffuse. In the case of

heterogeneous nucleation, the atoms diffuse until they reach a defect where they become trapped. If atoms are deposited on a terrace, they can diffuse until they reach a descending step edge. This barrier, also known as the step edge barrier, is both an energetic and physical obstruction to nucleation.   The energy barrier from the descending step edge can reflect the diffusing atom, while the ascending step edge can trap diffusing atoms. The diffusing atom is effectively trapped if its own energy is not great enough to overcome the barrier [19]. If the diffusing atoms are deposited at a steady rate, the step widths become uniform, as illustrated in Figure 8.

Figure 8. Atoms are deposited onto a stepped surface and get trapped at the descending step edges due to the Ehrlich-Schwoebel barrier, graphically represented below, forcing the steps to increase in size.
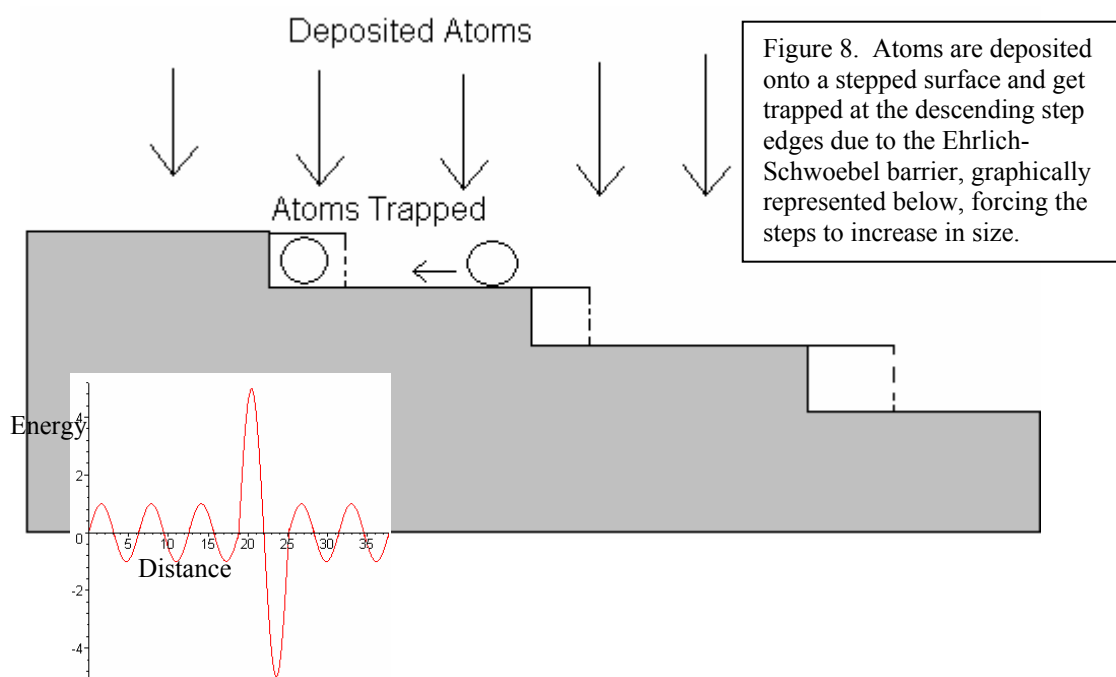
Preferential nucleation of Co on the Au (111) close packed surface has been studied by Morgenstern et. al. This group has found that Au(111), which reconstructs into a complex herringbone pattern, disperses the Co into nanoclusters. It was shown that the Co preferentially nucleates at the elbows of the herringbone pattern, creating regular arrays of islands. Figure 9 below shows increasing coverage of cobalt (a) 4% of a ML, (b) 12% of a ML, and (c) 28% of a ML. It is clear that the Co cluster size increases with

higher Co coverage. Even at higher Co coverage, the herringbone pattern remains and

coalescence of Co islands is not observed [17].
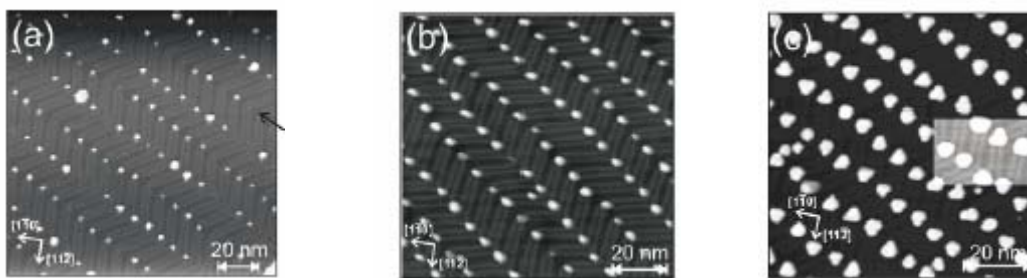
Figure 9. Preferential nucleation of Co on the herringbone surface is visible at different cobalt coverage, a) 4% of a ML, b) 12% of a ML and c) 28% of a ML [17].

Homogeneous, heterogeneous, and preferential nucleation occur when deposited

atoms diffuse on a surface and stick together forming clusters or nuclei. In homogeneous

nucleation, the surface on which the atoms diffuse is defect free. In heterogeneous

nucleation, the surface is considered to have defects. Preferential nucleation implies

there is a preferable surface site where the nuclei form. Utilization of preferential

nucleation of Co on an inert metallic surface may be the key in forming ordered magnetic

arrays useful for data storage.

Chapter 3

Materials

Rhenium is an important element with applications from catalysis to super conductivity. Rhenium, element 75, is a dense, hexagonal close packed transition metal. It is the substrate material used throughout this experiment. The surface orientation of this substrate is the $(12\bar{3}1)$. Rhenium was the last naturally occurring element to be discovered. At approximately one part per billion, rhenium is widely spread throughout the Earth's crust. Typically, a platinum-rhenium catalyst is used to make lead-free high-octane gasoline in a reforming process [22]. Catalysis refers to the acceleration of a chemical reaction by means of a substance that is not consumed by the overall reaction.

In the case of heterogeneous catalysis, the catalyst provides the surface on which the reactants are temporarily absorbed. (By adding nanostructures, this surface is changed.) The bonds in the reactants weaken enough for new bonds to be created. The bonds between the reactants and the catalyst are weaker than the bonds between the reactants, so the reactant product is released. Depending on the form of adsorption, Langmuir-Hinshelwood or Eley-Rideal mechanisms occur. In the Langmuir-Hinshelwood mechanism both molecules adsorb and react on the surface, while in the Eley-Rideal mechanism only one molecule adsorbs and reaction occurs when a gaseous molecule collides with it.

The reforming catalytic process takes straight chain hydrocarbons in the C_6 to C_8 range from the gasoline or naphtha fractions and rearranges them into compounds containing benzene rings. Hydrogen is produced as a by-product of the reactions.
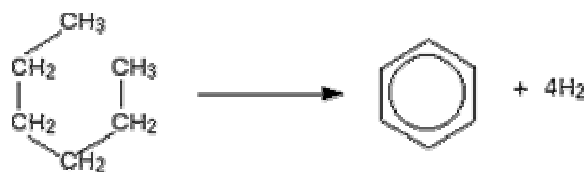
Figure 10. The reforming catalytic process transforms hydrocarbons into benzene rings and hydrogen.

Rhenium has the third highest melting-point of all elements, bested only by tungsten and carbon. The melting point of rhenium is 3459 K. For this reason, rhenium is often used in jet engine parts. Rhenium is also one of the densest elements, exceeded only by platinum, iridium, and osmium. Its density is 21.02 g cm^{-3}. Rhenium also has the largest number of oxidation states of any known element. Rhenium-molybdenum and tungsten-rhenium alloys are superconducting [22].

The rhenium crystal used in this study has a purity of 99.99%. It is approximately 10 mm in diameter. The thickness of the crystal is approximately 1.5 mm. The crystal is aligned within 0.5 degrees of the $(12\bar{3}1)$ orientation.

Previous experiments performed by Hao Wang have shown that after oxidation and annealing, facets will form on the rhenium substrate. The faceted oxidized rhenium surface is the proposed template for cobalt nanostructure growth. More detail on facet formation will be discussed in chapter 5.

Cobalt is the element used for formation of nanoclusters on faceted Re. Cobalt, element 27, has a hexagonal close packed structure [2]. It is a ferromagnetic element. This means that an external magnetic field can magnetize cobalt and the cobalt will remain magnetized for a period of time after it is removed from the magnetic field. The physical origin of this magnetization is from quantum mechanics, in particular, spin and the Pauli Exclusion Principle [12].

Cobalt's ferromagnetic properties make it an interesting element to study. In addition, cobalt nanostructures are of particular interest for high-density magnetic data storage [17]. A future experiment studying the ferromagnetic properties of cobalt nanostructures on a templated surface could be performed to aid in the understanding of how nanostructures affect the catalytic process.

Cobalt also has interesting catalytic properties. It is a major component of CoMo catalysts used for hydrodesulfurization. This catalytic process is used to remove sulfur from natural gas and from refined petroleum products like gasoline, kerosene, and diesel fuel. By removing the sulfur from the petroleum feed stocks, sulfur dioxide emissions from cars, trains, planes, etc. can be reduced [2]. In general, nanoarchitecture has been shown to enhance the selectivity, ability to produce one specific molecule out of a number of thermodynamically feasible products, of catalytic processes [25].

The goal of the present experiment is not to make catalysts or magnetic devices. Rather, it is to see how formulation of an oxygen-covered nanotemplate (faceted Re) affects the nucleation and growth of a sample vapor-deposited metal (Co). If we find evidence of preferential nucleation, it will have implications for other more useful metal/substrate combinations.

Chapter 4

Instrumentation, Cleaning Process, and Characterization of Techniques

The techniques of Low Energy Electron Diffraction (LEED), Auger Electron Spectroscopy (AES), and Scanning Tunneling Microscopy (STM), which were used to acquire data for the majority of this thesis, are described in the following sections. These procedures are highly surface sensitive and frequently used to study surfaces and surface processes.

4.1 Experimental Setup

The chamber used for this experiment is a stainless steel, ultrahigh vacuum (UHV) chamber. The base pressure is 2×10^{-10} Torr. The benefits of using a UHV chamber are atomic cleanliness and the generation of a long mean free path for the particle beams used for measurements. The particles from the particle beam require a path greater than 20 cm to travel across the chamber without collision with a gas molecule. A metal evaporator provides the primary source of cobalt. It is deposited on the substrate's surface by thermal evaporation. The rate of cobalt deposition is approximately 0.20 ML/min estimated from Auger spectroscopy studies.

In the center of the chamber is an X-Y-Z rotary manipulator. In addition to the X, Y, and Z transitional movement, a fourth degree of freedom is permitted allowing a 360 degree rotational movement. The manipulator provides a means to transport the sample to various locations in the chamber as all the experimental equipment is not located in the same place. The manipulator even provides means to transfer the sample holder assembly to the scanning tunneling microscope's measurement platform.

To measure the pressure in the chamber, an uncalibrated Bayard-Alpert ionization gauge is used. A filament for electron bombardment heating of the Re sample is biased to a high voltage (-1.5 kV) and is located behind the substrate surface. Another filament is located in the chamber and is typically used for cleaning purposes.

Figure 11. This is the chamber that was used to conduct the experiments for this thesis.

Ionization Vacuum Gauge

Rear View Low Energy Electron Diffraction (LEED) Optics

Sample Manipulator and Holder

Cobalt Evaporator

Scanning tunneling Microscope (STM)

Auger Electron Spectroscopy (AES) Assembly

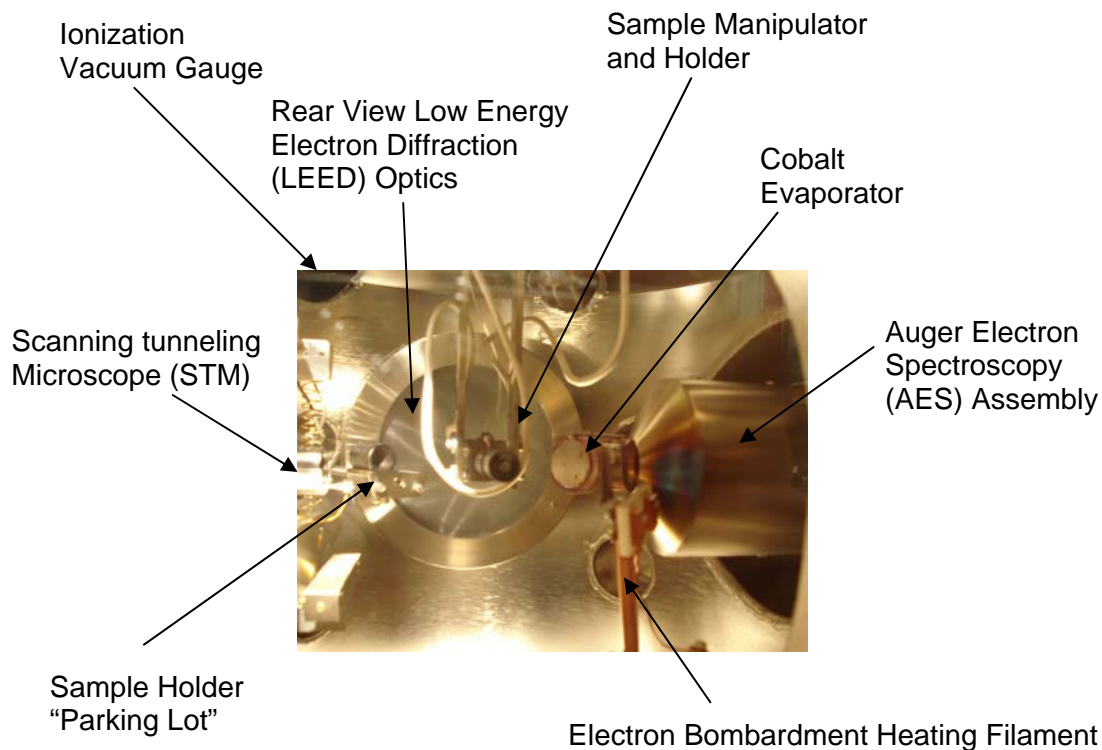Sample Holder "Parking Lot"

Electron Bombardment Heating Filament

Figure 12. Looking through the front view port, the inside of the chamber and all of the equipment used for this thesis is visible.

4.2 Sample Cleaning

Cleanliness is highly important when studying the physical and electronic properties of a surface. The presence of impurities affects the physical properties of the surface studied. After heating a crystal to high temperatures, bulk impurities will often find their way to the surface [30]. Sulfur, nitrogen, oxygen, and carbon are the particular impurities found on the Re crystal used in this study. The sulfur and nitrogen contaminants are the results of previous experiments performed in the UHV chamber used for this study.

The oxygen contamination is not a particular problem, as the surface requires oxygen to induce faceting. The carbon impurities, however, inhibit the faceting process and must be reduced as much as possible. To remove the carbon surface contaminants, flash heating in oxygen is required. The carbon reacts with the oxygen to desorb as CO. The remaining oxygen on the surface is not a problem due to the reasons described above.

To clean a sample, an electron beam is used to heat the sample to temperatures greater than 2200K. In order to complete this process, a filament is positioned in front of the sample and a current is applied to the filament in order to remove contaminants from the surface. This heating procedure is continued until the Auger spectrum shows low levels of contamination. If the residual contaminant species, mainly carbon, are smaller than a few percent of a monolayer of atoms, the experiment is continued. The cleanliness of the surface is double checked with LEED patterns. The typical conditions used for e-beam cleaning are provided in chapter 6, section 2.

4.3.1 Low Energy Electron Diffraction

The highly surface sensitive method known as low energy electron diffraction (LEED) is used to investigate the periodic arrays on the surface of a crystal. Making use of the de Broglie relation, this method uses electrons to hit the crystal's surface with a wavelength approximately 0.64 to 3.9 Angstroms and electron energies from 20 eV to 800 eV. This size wavelength is a good match for interatomic spacing on surfaces. The mechanism behind this technique is as follows: low energy electrons bombard the crystal surface resulting in both elastic and inelastic scattering. Since the mean free path of the inelastic scattering is on the order of 5 to 10 Angstroms, the elastically backscattered electrons dominate the system and are diffracted onto a fluorescent screen. The backscattered electrons reveal the surface lattice structure in reciprocal space on the screen. The relationship between the unit cell in real space and reciprocal space is logical: the distance, d, between atoms in a unit cell in real space transforms to the reciprocal of that distance (1/d) in reciprocal space. Using conservation of energy and momentum, one can determine the surface structure of a crystal [29].

The wavelength of the electron is defined by the de Broglie relation:

$$\lambda = h/p,$$

where h is Planck's constant, and p is momentum. From the definition of momentum a relationship between electron energy and wavelength can be derived,

$$p = mv = (2\ m_e E_K)^{1/2}\ ,\quad \lambda = h/(2\ m_e E_K)^{1/2}$$

where m_e is the mass of an electron, v is velocity, and E_K is the kinetic energy of the electron. If the incident electron approach the surface from the normal direction and

scatter from the surface with angle θ from the surface normal, the path length difference

can be defined as

$$d= a \sin \theta,$$

where a is the distance between atoms in a one-dimensional periodic array at the surface.

When the path length difference is an integer multiple of the electron wavelength,

constructive interference occurs. This is known as the Bragg condition, given by the

following formula:

$$a \sin \theta=n \lambda,$$

where n is an integer [29].

Using the derivation above, the diffraction pattern for a 2-D array can be

obtained. The figure below, Figure 13, illustrates a surface unit cell contained by vectors

a_1 and a_2. The electron wave is depicted by the incoming vector $\overline{K}$ and the outgoing

vector $\overline{K'}$.

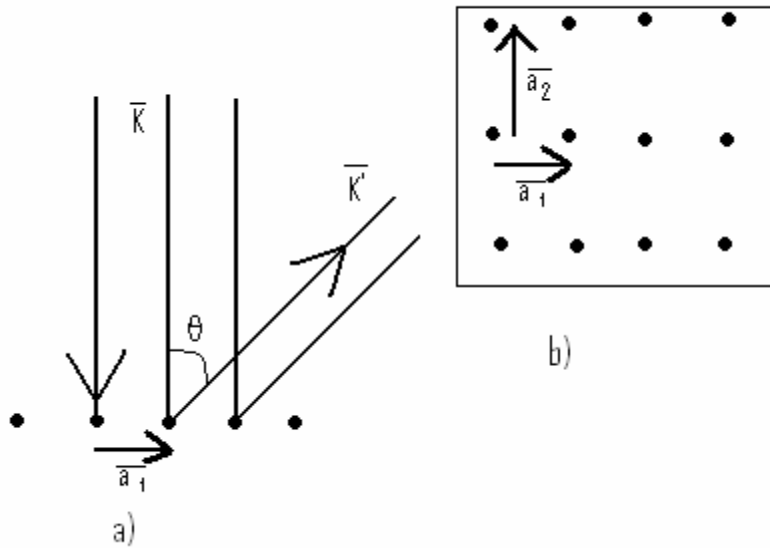Figure 13. a) Schematic of diffraction from a 1-D array of atoms b) A surface
unit cell of a rectangular array of atoms, with lattice vectors a_1 and a_2

The equation derived previously, using Bragg's condition can now be extended for interference in 2 dimensions as follows:

$$a_i \sin \theta = n \lambda \,,$$

$$(a_i \sin \theta)(2\pi/ \lambda) = 2\pi n,$$

$$\overline{a}_i \bullet \overline{K}' = a_i \ K' \sin \theta = a_i \ (\frac{2\pi}{\lambda}) \sin \theta$$

where i = 1 or 2, n is an integer, and vectors $\overline{a}_i$ and $\overline{K}'$ are defined by Figure 13. The equation above is satisfied by the condition:

$$\Delta \overline{K}'_{\parallel} = (\overline{K}' - \overline{K})_{\parallel} = 2\pi(n\overline{g}_1 + m\overline{g}_2)$$

where n and m are integers that fulfill Bragg's condition and $(1/a_i) = g_i$ is the reciprocal unit cell vector.

In principle, one can make careful current and voltage measurements of the LEED beams and fit the data using multiple scattering theory to obtain the surface structure. In the present case, LEED is used to identify the symmetry of the surface unit cell to determine surface cleanliness and to tell whether or not facets have formed.

By varying the energy range of the electron gun, facets can be observed. To perform this procedure, pictures of LEED patterns are taken at different electron energy values. As the electron energy is increased, the constructive diffraction pattern spots move toward specular poles. On the faceted $Re(12\overline{3}1)$ surface, two specular poles are observed and are associated with the $(01\overline{1}0)$ and $(11\overline{2}1)$ facets. These same two poles are observed after oxygen is dosed on a faceted $Re(12\overline{3}1)$ surface [29]. Princeton

Research Instruments' four grid rearview low energy electron diffraction optics were used for the measurements performed in this experiment.
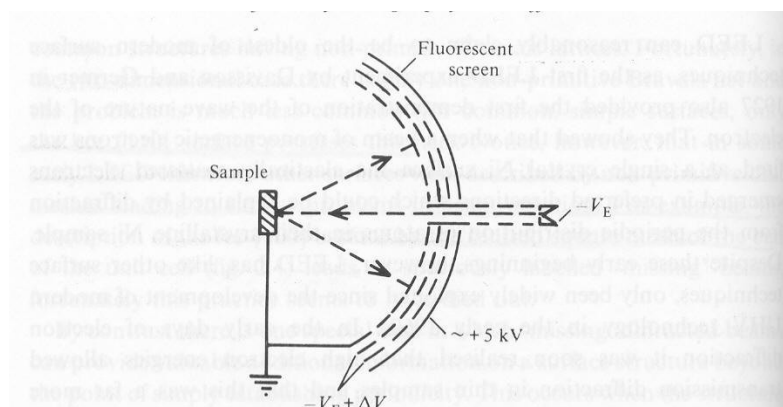

Figure. 14. A schematic diagram [29] shows the LEED optics. Low energy electrons are created by the electron gun and scattered by the surface of the sample. The diffracted electrons are collected on a +5 kV fluorescent screen. The $-V_E$ potential is used to bias the filament of the electron gun, while the $-V_E + \Delta V$ potential is required to retard the inelastically diffracted electrons.

4.3.2 Auger Electron Spectroscopy

To understand the chemical composition on the surface of a sample, Auger Electron Spectroscopy (AES) may be utilized. The Auger process is the prime mechanism of AES. The process entails a beam of electrons hitting surface atoms on a sample after which an electron is excited out of the inner atomic level if its binding energy is less than the incident beam energy. This excitation ionizes the atom leaving an electron vacancy available to be filled by another electron from a higher energy state by de-excitation. When the second electron de-excites, energy is released and is then transferred to a third electron in the atom. If the energy transferred is great enough to overcome the binding energy of the electron, it can lead to the electron being ejected into the vacuum and collected by an analyzer. The energy can be characterized by the following equation:

$$E_{Auger} = E_A - E_B - E_C - U \; ,$$

$$U = H - P$$

where E_A (core state energy), E_B (outer shell state energy), and E_C (outer shell state energy), are illustrated in the electron levels in the image below, H is the hole to hole interaction energy, and P takes into account the extra-atomic relaxation energy effects of the solid state environment [29] .

Figure 15. Schematic of the Auger process [29].
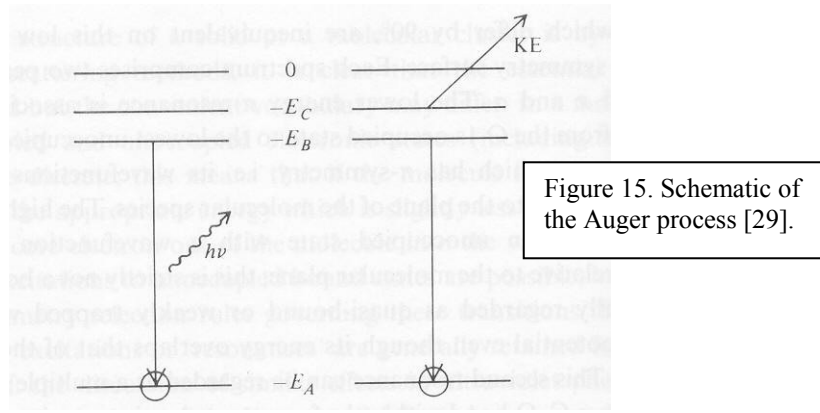
The primary electron beam penetrates the surface deeply, creating Auger electrons below the top few surface layers, which in turn creates background noise in measurements because the measured Auger electrons come from the top few surface layers. The reason the technique is highly surface sensitive is due to the short inelastic electron scattering mean free path.   The sensitivity of this technique is typically a few hundredths of a monolayer for impurities such as carbon and oxygen [29].

A Physical Electronics single pass cylindrical mirror analyzer with an integral electron gun as the electron source was used in this experiment. Incident electrons hit the sample surface along the surface normal direction. The detected Auger electrons are collected at 46 degrees from the surface normal. The collection angle is important

because it reduces the effective escape depth of the Auger electrons by a factor of cos(46 degrees).

Auger spectra are typically used for qualitative identification of surface species. If the elemental sensitivity factors are known it is possible to quantitatively determine the amount of a present surface species. By comparing the peak height intensities from two separate Auger spectra, an estimate of the relative concentration of a surface species (cobalt) can be determined.

By assuming 1ML of cobalt covers the Re surface, the following formula can be used to give a rough estimate of coverage:

$$I_{Re}/I_{Re\ Clean} = \exp(-d_{Co}/\lambda_{Re}) = 0.49,$$

λ = inelastic mean free path (λ_{Re} = 3.5A)
d = diameter of atom (2.5 A for Co)
E_{Re} = 176eV
I = Intensity

where I is the peak intensity at E_{Re}, d is the diameter of a Co atom, and λ_{Re} is the attenuation length through the Co. From Figure 17, this peak ratio corresponds to approximately 5 +/- 1 minute to cover the surface in 1ML.
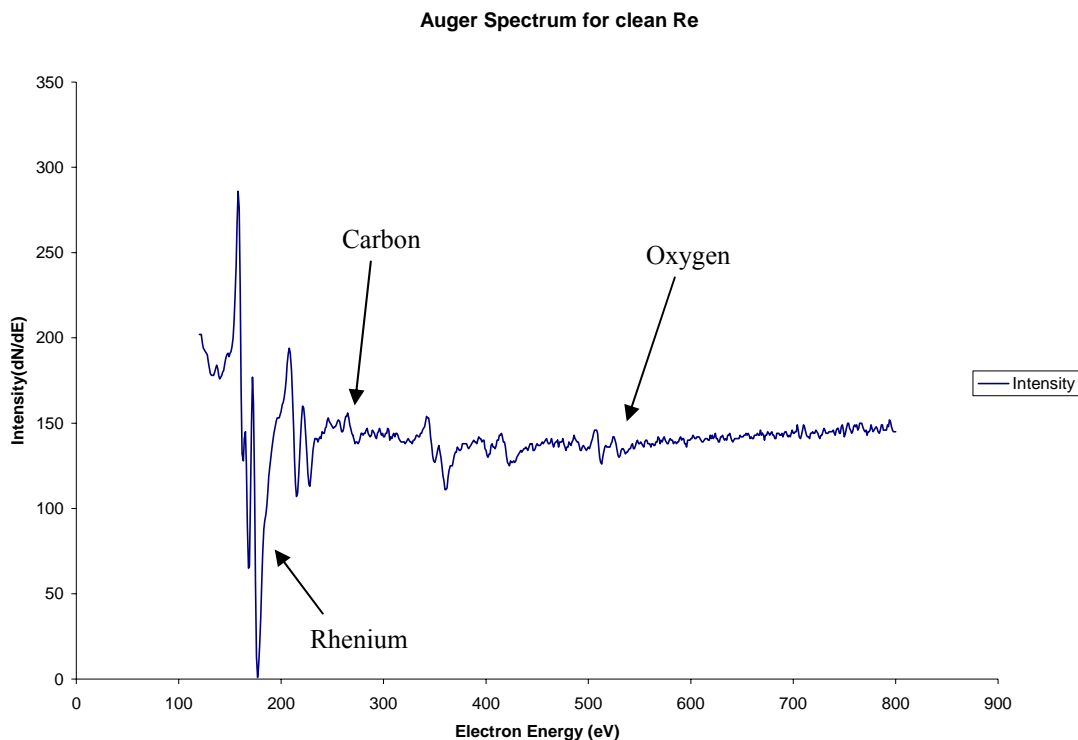
Auger Spectrum for clean Re

Figure 16. This is an Auger spectrum for clean Re. The spectrum shows a little contamination from carbon and oxygen.

If the coverage is formed layer by layer, a graph of the coverage versus time would be linear for the first monolayer. If linearity is not the case, clustering may be a cause [29]. The figure below, Figure 17, was compiled using a basic model for electron attenuation length through 1 ML of cobalt. The normalized Re(176 eV) peak to peak intensities from six separate experiments are plotted in Figure 17.
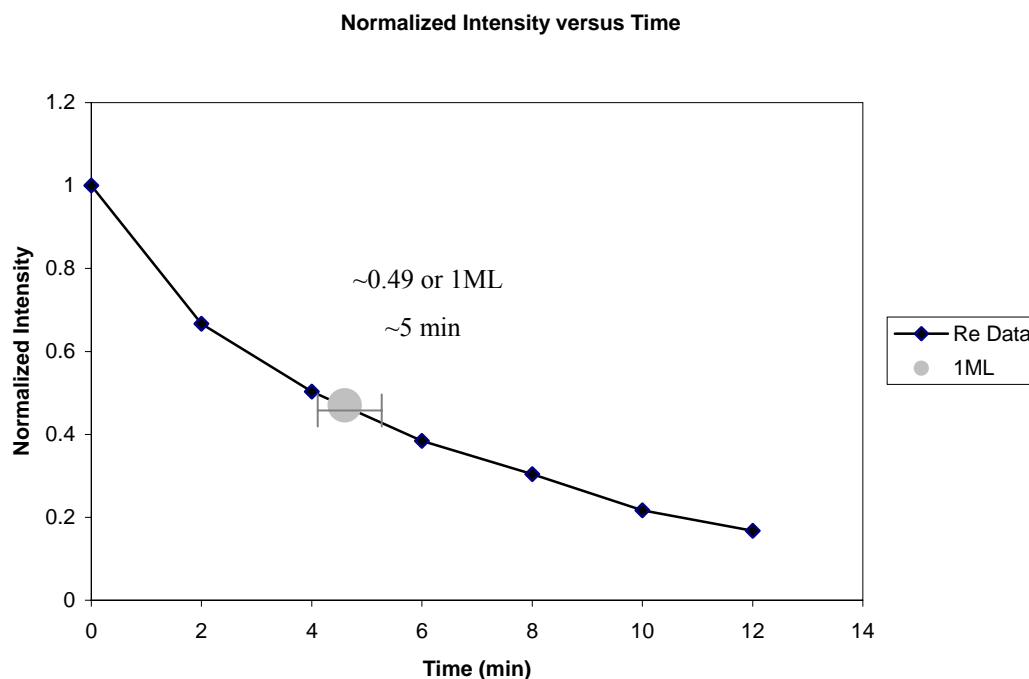
Normalized Intensity versus Time

Figure 17. This graph was created by estimating the electron attenuation length for 1ML of Co on Re(11-21). From this graph estimates of cobalt coverage are made for the entire paper.

4.3.3 Scanning Tunneling Microscopy

A McAllister UHV Scanning Tunneling Microscope (STM) was used to acquire the majority of data in this study.   The STM allows a user to access real-space morphology of solid surfaces with atomic resolution. It can be used to create nanoscale objects as well as manipulate individual atoms.   In this study, the STM was used to probe the rhenium surface for cobalt.

An optically sharp tip is mounted such that it can be manipulated via an electrically controlled piezo material to move in the X, Y, and Z directions. The tip moves line by line across the surface, scanning it. The scanning records the differences between local electronic states. The electronic states are explored using a quantum

tunneling current (1 nA) between the tip and the neighboring region of the surface; a bias

voltage (1V) spans the gap in between [29].

There are two modes of scanning for the STM. In the "constant current" mode,

the tunneling current is kept constant by adjusting the height of the tip with respect to the

surface through a feedback circuit. The STM electronics receive information regarding

the tunneling current and adjust the height to maintain a constant current by sending an

electric voltage to correct the tip position. The tip motion is then recording imitating the

contours of the surface morphology of the electronic states. When all of the scan lines

are mapped together, a real-space image of the surface is created [29].

The other mode of scanning is the "constant height" mode.   In this case the

tunneling current is recorded as a function of the tip location on the scanned part of the

surface. The height of the tip from the surface is fixed regardless of whether it may crash

into a feature protruding from the surface. To obtain information on surface morphology,

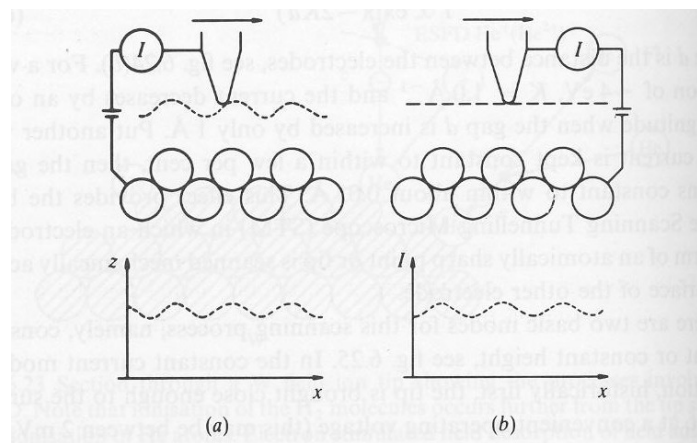the tunneling current is utilized [29].

Figure 18. Image [29] (a) illustrates the atomically sharp STM tip
probing the surface in constant current mode, while (b) shows the STM
tip probing in constant height mode.

The complex tip-substrate interactions create challenges when quantifying data collected through scanning tunneling microscopy. A simple model for understanding the interaction is shown in Figure 18. A conducting sample and a metal tip are separated by a vacuum gap of distance d. By applying a positive bias between the (positively charged) sample and (negatively charged) tip, the Fermi level of the tip is raised with respect to that of the sample. Assuming a small bias and elastic tunneling, the resultant tunneling current in this case is equal to the total number of electrons per unit time that cross the work function barrier from the tip's filled states and tunnel to the available unoccupied states of the sample [29].

The electron wave function at the Fermi level (the highest filled level in a conductor at 0 K) escaping the confines of a potential well can be characterized by an inverse exponential decay. When two of these potential wells are brought close together and a voltage is applied, a current can flow between them; the overlapping wave function allows for this quantum mechanical tunneling. The work function is defined as the difference between the electrochemical potential energy of an electron just inside a conductor and the electrostatic potential energy of an electron in the vacuum just outside. At low voltages the tunneling current can be approximated by:

$$I \sim \exp(-2Kd),$$

where $K = (2\pi/h)(2m\phi)^{(1/2)}$, h is Planck's constant, m is the mass of an electron, ϕ is the effective local work function, and d is the distance between the tip and the substrate [29]. Typical values of ϕ and d are 4 eV and 5-7 Å respectively.

The STM tips used in this study are made from tungsten etched from 0.25mm wire and are approximately 1 cm long. If a tip is damaged, it can be replaced in situ with

a wobble-stick designed specifically for tip changing. The tips used for this experiment were purchased from Custom Probes Unlimited.

Figure 12 illustrates the McAllister UHV STM with the sample holder assembly on the conducting rails. Before measurements can be made, the STM device must be isolated from vibrations. To accomplish this task, the STM platform is detached from the base plate by unscrewing the clamp. This leaves the entire STM platform supported by four springs to provide dampening from interfering vibrations. Due to the size of the gap between the tip and surface, isolation from any vibrations is imperative. If vibrations occur during measurement, the results can range from invalid data to surface destruction due to the tip crashing into the surface [29].

After the platform is isolated, the sample holder assembly is moved along the conduction rails. An optical microscope is then used to finely adjust the location of the sample holder, guiding the final stage of the motion. A programmed sequence of tip and sample movements is used to establish a tunneling current.

During the scanning process (sometimes before scanning can begin), the tip becomes dirty. The software provided with the STM has a "bias pulse" function and is used for cleaning dirty tips. A pulsed bias can be applied to the tip-surface in junction with a preset voltage between -10 V and +10 V. (Obviously, this technique can lead to surface degradation and should be performed near an isolated area of the surface.) Another method for cleaning the tip comes from scanning a non-interesting part of the surface very quickly. This rough treatment of the tip is designed to drop extra atoms from the tip or pick up adatoms from the surface in hope of creating an atomically sharp tip.

Despite problems with tip cleanliness, chamber vibrations, and establishment of a tunneling current, the McAllister UHV STM is a very powerful tool for surface morphology imaging. Figure 19, below, is an image taken on a Re(11-21) surface dosed with approximately 1.3 ML of cobalt. It appears from this image that clustering is occurring on the surface.   STM, in conjunction with AES, becomes very powerful for surface characterization.

Figure 19. This 1000 Å x1000 Å STM image confirms clustering is occurring on the rhenium surface.
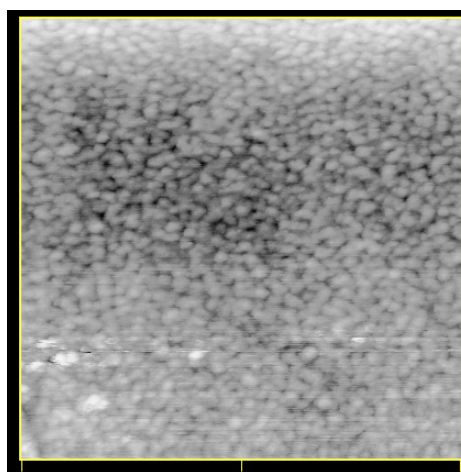
Chapter 5

Oxygen Induced Faceting of Rhenium($12\bar{3}1$)

A myriad of experiments have been conducted driven by the desire to understand the nature of adsorbates, substrates, and surface free energy. If the anisotropy of the surface free energy is enhanced by adsorbates covering the substrate's surface and annealing, facets may form minimizing the total free surface energy. The process of forming facets in this manner is thermodynamically driven, involving mass transport of immense quantities of atoms. The size and shape of the facets is determined by nucleation rates and diffusion rates [28].

Surface free energy,γ, is defined as the reversible work necessary to create a surface, and is expressed as energy per area. For a solid the surface free energy is proportional to the cleavage energy and is roughly the energy necessary to break surface bonds. A typical surface free energy for a solid is approximately 1200 ergs/cm^2 or 1.2 J/m^2. The equilibrium shape of small crystals can be determined from anisotropy in surface free energy. The crystal will seek a shape that minimizes the integral:

$$\oint \gamma(\theta)\, dA$$

at constant volume: this is Wulff's theorem [32].

The orientation ($12\bar{3}1$) is chosen because it is atomically rough (see hard sphere model in Figure 20 a and b). As shown in a stereographic projection, Figure 20 c, the ($12\bar{3}1$) orientation is near the orientations ($11\bar{2}0$), ($01\bar{1}0$), ($011\bar{1}$), and ($112\bar{2}$), which could potentially be facets. Atomic roughness is important because this surface has a

greater surface free energy than more close-packed Re surfaces. Clean planar rhenium does not form facets spontaneously. Oxygen is necessary to increase the anisotropy of the surface free energy, as discussed in more detail in the following pages [21,27]. Rhenium has a hexagonal close packed structure with unit cell parameters a=2.716 Å and c=4.458 Å [10]. The unreconstructed Re(12$\bar{3}$1) surface has six layers of atoms exposed and the "top-layer of atoms shows a quasihexagonal arrangement", as seen in Figures 20 a and b.
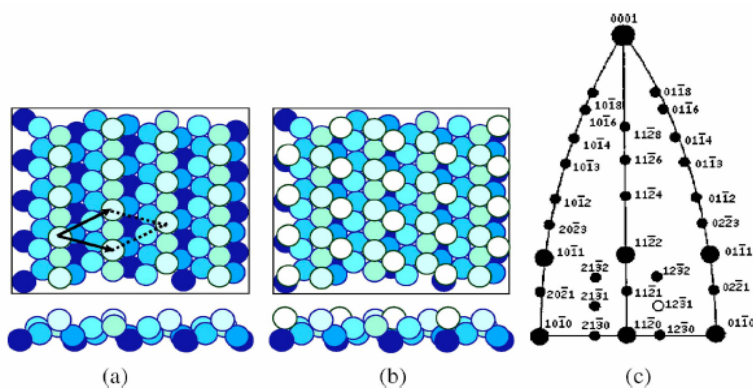

Figure 20. The hard sphere model [28] depicts the atomic organization of Re(12$\bar{3}$1) both a top view (a) and a side view (b) are provided. A stereographic projection showing the crystallographic location of the Re(12$\bar{3}$1) surface is provided in (c).
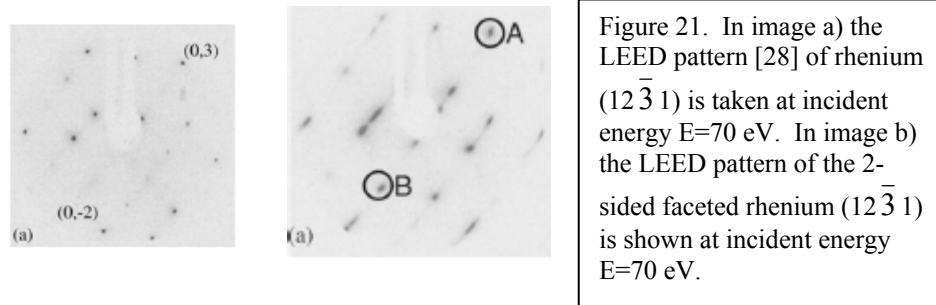
The experimental procedure used to create a faceted rhenium surface by Wang et. al.[28] was also used in this study. The Re crystal is cleaned by electron beam heating in oxygen (1 x10^{-7} Torr) and then flashing the crystal to temperatures of approximately 2000 K. The cleanliness of the surface is then checked by AES. After the surface is cleaned, oxygen is dosed onto the Re surface at room temperature. This is accomplished by backfilling the chamber and monitoring the change in pressure through the use of a Bayard-Alpert ionization gauge. The Re crystal is then annealed while the temperature is monitored using an infrared pyrometer. After the facets are created, the O_2 coverage is

confirmed by AES measurements and the facets are confirmed by LEED. Next,

extensive STM scans are performed [28]. Other surfaces such as W(111), Mo(111), and

Ir(210) have been shown to have ridge like morphology under absorbate-induced faceting

conditions [5,15,18]. In particular, W(111), a body centered cubic, has been the most

carefully studied [14,15].

The procedure mentioned above is one way to create a faceted surface. The

largest facets used in this experiment were generated by three or four, ten second

sequential e-beam heatings to temperatures greater than 2200K of Re(12$\bar{3}$1), followed by

cooling in O_2 at a pressure of $1x10^{-7}$ Torr. Further detail is provided in chapter 6

regarding the experimental procedure used to create the faceted surfaces used in this

experiment.

By using the methods discussed in Chapter 4, the O/Re Auger peaks are used to

determine the coverage of the oxygen. The amount of oxygen dosed is measured in

Langmuirs, L, where $1L=1x10^{-6}$ Torr $*s=1.33x10^{-4}$ Pa$*$s. Oxygen saturates the surface

between 5 and 7L or approximately 1 ML (1ML= $1x10^{15}$ atoms/cm^2). After AES is used

to confirm the oxygen coverage, LEED is performed to confirm the faceting [28].

A typical LEED pattern from a clean Re(12$\bar{3}$1) surface is illustrated in Figure 21

a. Upon increasing the incident electron energy, the low energy electron diffraction spots

converge to the center of the screen. This event signifies a planar surface despite the

atomic roughness. Even after annealing a clean Re(12$\bar{3}$1) surface, no new features in the

LEED diffraction pattern are discovered [28].

Figure 21. In image a) the LEED pattern [28] of rhenium $(12\bar{3}1)$ is taken at incident energy E=70 eV. In image b) the LEED pattern of the 2-sided faceted rhenium $(12\bar{3}1)$ is shown at incident energy E=70 eV.

The following table summarizes the different surface structures that occur after dosing the $Re(12\bar{3}1)$ surface with different oxygen coverage and then annealing it to different temperatures:

Oxygen Dose (d)	Annealing Temp (T)	Surface Structure
d < 0.5 L	T< 2000 K	Planar
0.5L < d < 1L	T > 700 K	Tiny facets coexisting with $(12\bar{3}1)$ surface
1 L < d < 3L	T > 700 K	Two facets $(01\bar{1}0)$ and $(11\bar{2}1)$
d ~3L	T = 1000K	Three facets $(01\bar{1}0)$, $(11\bar{2}1)$, and $(10\bar{1}0)$
d ~10 L	T = 900K	Four facets $(01\bar{1}0)$, $(11\bar{2}1)$, $(10\bar{1}0)$, and $(01\bar{1}1)$

Table 1. This table summarizes the experimental conditions leading to different facet formation.

The surface covered by ridges defined by the two facets $(01\bar{1}0)$ and $(11\bar{2}1)$ form the template used for this study. The LEED pattern for a surface with these two- sided facets is shown in Figure 21b. The diffraction spots from the faceted LEED pattern do not converge to the center of the screen as the electron energy is changed. However, the diffraction spots do move toward either of the fixed spots marked by A and B in the image. The fixed spots are specular poles associated with the facets $(01\bar{1}0)$ and $(11\bar{2}1)$. The orientation of the two facets is determined by comparing the planar LEED pattern with the faceted LEED pattern. Using an Ewald Sphere[29], the tilt angles between

spectral poles associated with A and B taken with respect to the Re(12$\bar{3}$1) norm can be calculated. The angles were determined to by 22.2 degrees and 12.0 degrees. Based on these measurements and calculations the Miller Indices of the facets were identified [28].

Atomic resolution STM images and kinematical simulations provide strong evidence for the assumption that all the facets have the "ideal bulk-truncated structures." It is clear from the atomically resolved STM image, Figure 22, that herringbone structures exist on the surface. The upper facet of the herringbone structure relates to the (01$\bar{1}$0) facet, as illustrated in the hard sphere model. The bottom of the herringbone structure is not as well resolved as the upper facet, but some atoms are visible. This side corresponds to the (11$\bar{2}$1) facet as illustrated in the hard sphere model. It is important to note that the edges along the [$\bar{2}$113] direction are atomically sharp [28].
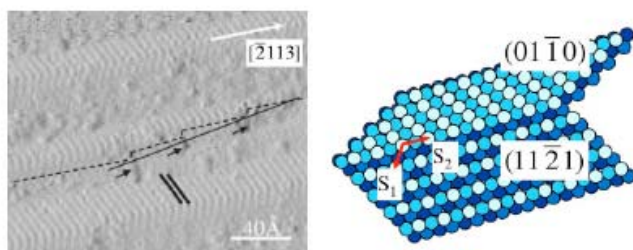

Figure 22. This atomically resolved STM image shows the herringbone structure of the (01$\bar{1}$0) facet. A hard sphere model is provided for comparison [28].

The final facet size is controlled by several elements: coverage of the adsorbate (oxygen), annealing temperature, and annealing time. For constant oxygen coverage and annealing time, the facet size grows as the annealing temperature increases. When oxygen coverage and annealing temperature is constant, the facet size increases as the annealing time increases. Increasing the oxygen coverage, while keeping the annealing temperature and time fixed, shows a trend of decreasing ridge length and relatively

constant ridge width. Typical ridge length varies from 50 Å to 450 Å and typical ridge width varies from 10 Å to 200 Å. The ridges have been observed to last up to a week without morphological changes [28].

Thermodynamics and kinetics are the general causes of faceting. The primary driving force for surface faceting is an anisotropy of the surface free energy. In order for facets to form, all the thermally stable facets must be present and the faceted surface's total free energy must be smaller than the total surface free energy of the original planar surface [11]. In the case of clean metal surfaces, the anisotropy of the surface free energy is not great enough when annealed to cause faceting [4,13]. By covering a metal planar surface with an adsorbate, the surface free energy is generally decreased and may, upon annealing, cause faceting. The energetic requirements for faceting of Re($12\bar{3}1$), ignoring edge energies, are calculated by:

$$\sum_i \frac{\gamma_i}{\cos\theta_i}\lambda_i - \gamma_{(12\bar{3}1)} < 0,$$

"where θ_i is the tilt angle between facet i and the ($12\bar{3}1$) plane, λ_i is the structural coefficient describing the partial contribution of facet i to the total projected area on ($12\bar{3}1$) by all the facets, and γ_i is the surface free energy of facet i per unit area [28]." From the equation above, it can be determined that the facets that have the smallest surface free energy of facet per unit area and tilt angle are more favorable and thus likely to form [1,24,27,31].

In summary: adsorption of oxygen on Re($12\bar{3}1$), followed by annealing to an elevated temperature, induces morphological changes. Different oxygen coverage leads to different facet formation. For 1L to 3 L of dosed oxygen and annealing to

temperatures less than 700K, the surface becomes completely faceted with $(01\bar{1}0)$ and $(11\bar{2}1)$ facets. The distance between facets, or facet width, is relatively uniform and the edges are atomically sharp [28].

Chapter 6

Preferential Nucleation of Co Nanoclusters on Re($12\bar{3}1$)

6.1 Introduction

The initial goal of this study was to discover the conditions under which cobalt nanowires would nucleate on the faceted O/Re($12\bar{3}1$) surface. However, by annealing the cobalt after deposition, nanoclusters were observed. In order to guarantee that all experiments were performed under well defined conditions, the surface cleanliness and coverage were monitored by AES.

6.2 Cleaning

Cleanliness is important when studying the physical and electronic properties of a surface. In order to ensure a clean surface is used for each experiment, the cleaning procedure in chapter 4 is followed. The typical electron bombardment conditions for flash heating the sample are a voltage of 2.0 kV, a current of 100 mA, for a duration of 15 seconds.

6.3 Experimental Results

Four different experiments were performed that achieved scientifically interesting results. The first two experiments showed that Co nanoclusters preferentially nucleate in the trenches of the faceted Re($12\bar{3}1$) surface. The third and fourth experiments showed that the Co nanoclusters could be controlled in size, while still preferentially nucleating in the trenches of the faceted Re($12\bar{3}1$) surface. The table below summarizes the

experimental conditions used for the four experiments that are elaborated on in the
following section.

Exp. #	Co Coverage	Annealing Temp	Facet Width	Facet Height
1	3 +/- 0.4 ML*	T= 800K	~20 nm	~28.0 Å
2	3 +/- 0.2 ML	T= 800K	~20 nm	~28.0 Å
3	1.6 +/- 0.2 ML	T< 680 K	~10 nm	~15.0 Å
4	1.6 +/- 0.2 ML	T< 680 K	~10 nm	~15.0 Å

Table 2. This table summarizes the experimental conditions used to make and vary cobalt cluster size. * Two sequential deposition of Cobalt were performed.

After the surface is thoroughly cleaned, the real experiment begins. Surface
preparation is critical for preferential nucleation. Initially, a faceted O/Re(12$\bar{3}$1) surface
is created. In experiment 1 and experiment 2, the procedure used to create this faceted
surface was similar to the one explained in Chapter 5. Approximately 33L (1 x10^{-7} Torr
for 5.5 min) of oxygen was dosed by backfilling the chamber and monitoring the change
in pressure through the use of a Bayard-Alpert ionization gauge. During the dosing
process, the surface was e-beam heated four times for approximately 10 seconds each
time to a temperature greater than 2200K. Upon cooling in oxygen, a faceted surface
with two facets (01$\bar{1}$0) and (11$\bar{2}$1) was observed. The average width of the facets was
approximately 20nm and the facet average height was approximately 3nm.

The surface was then dosed with another 10L of oxygen causing an oxygen
saturation of the surface. This step minimizes the possibility of cobalt directly bonding
with the rhenium. At this point an AES measurement was taken to confirm that the
surface was saturated in oxygen. Then a LEED measurement was performed to confirm

the surface was properly faceted. In experiment 1, two sequential dosings of cobalt were performed. The first cobalt dosing provided 1 ML +/- 0.2 ML of cobalt and the second dosing provided 2 ML +/- 0.2 ML of cobalt coverage. The total cobalt coverage was approximately 3.0 ML. AES and LEED measurements were performed again to confirm the cobalt coverage and that the facets still remained. Finally, the Co/O/Re($12\bar{3}1$) faceted surface was gently annealed to a temperature of approximately 800K for 3 minutes.

It appears from the image, Figure 23, that the surface is covered in cobalt clusters. Since this image was rendered after x-slope was taken, the true height of the surface features is estimated from the image prior to having the x-slope taken. The approximate heights of the facets are 28 Å.
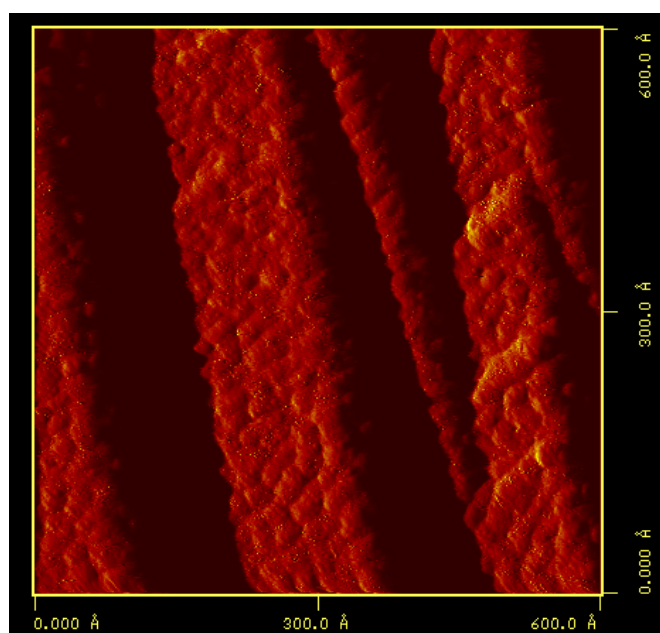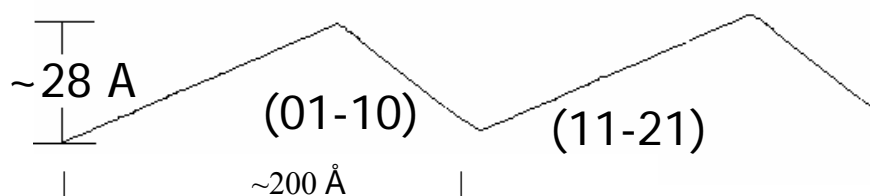

Figure 23. In this 600 Å x 600 Å STM image it is clear that the O/Re is faceted and covered in cobalt clusters following deposition of 3ML of cobalt at room temperature. The bottom image shows the height scale of the faceted surface.

~28 A   (01-10)   (11-21)

|_____ ~200 Å ____|

Gently annealing the surface gave the cobalt the mobility needed to form nanoclusters, as seen in Figure 24. These were the original conditions that led to the discovery of Co nanoclusters on the rhenium surface. This experiment was performed twice, experiment 1 and experiment 2, to confirm that the results were accurate and reproducible.
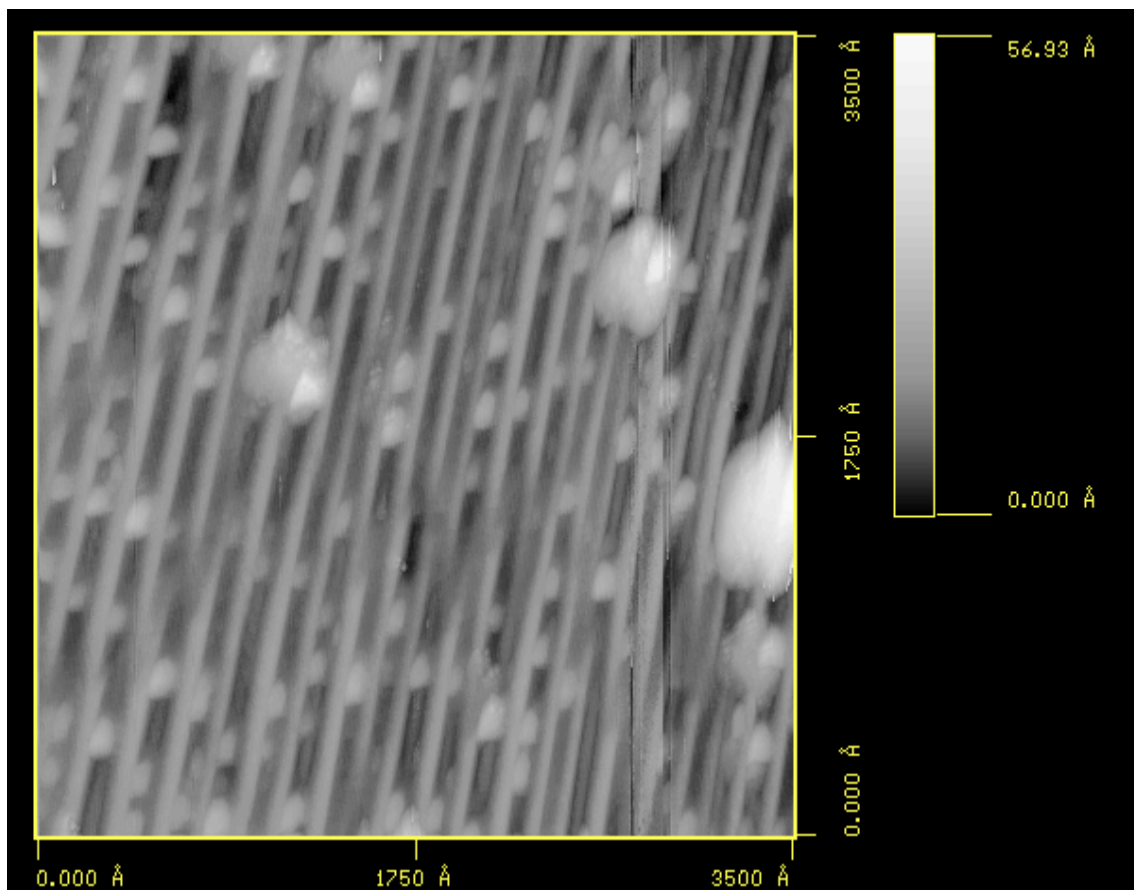

Figure 24. First Experiment
After annealing cobalt covered surface, preferential nucleation in the facet trenches of cobalt nanoclusters is clear from this 3500 Å x 3500 Å STM image. The large clusters may be formed by contaminants on the surface. They are not taken into account in the cluster statistics to follow.

From STM image analysis it is clear that the nanoclusters preferentially nucleate in the trenches of the $(01\bar{1}0)$ and $(11\bar{2}1)$ facets. Scan line analysis of the STM images

confirm what the eye sees; the Co nanoclusters do not spill over the edges of the facets, but are in fact contained between the two facets.
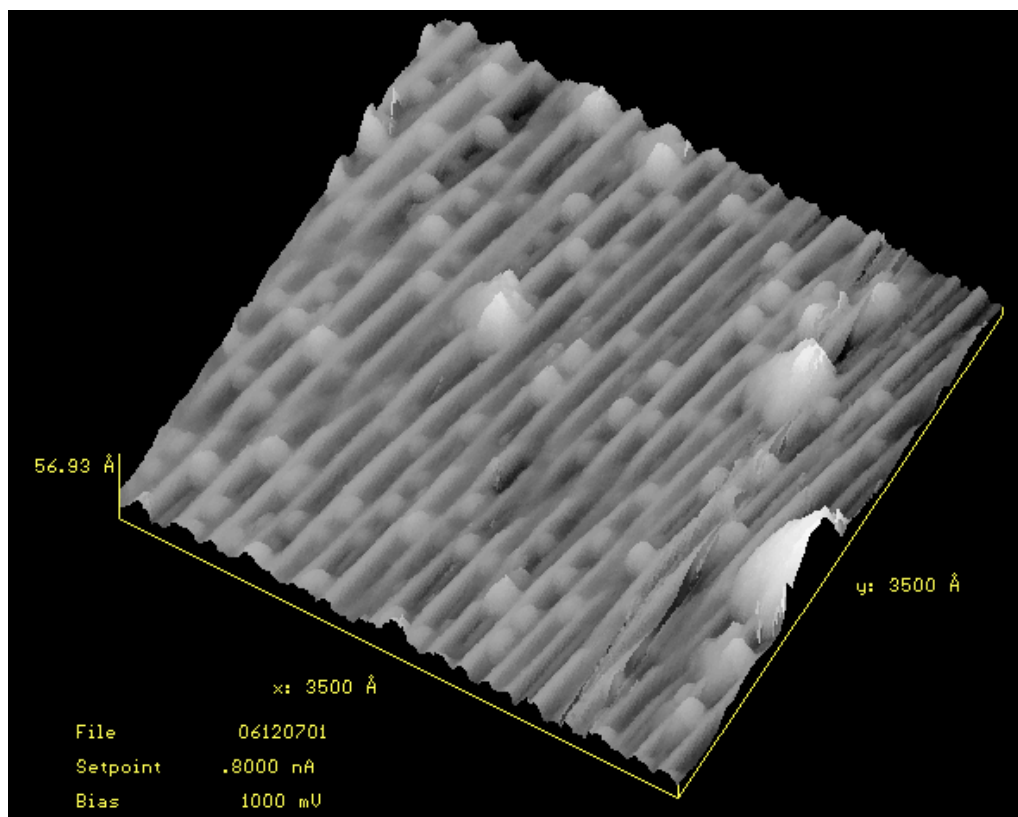

Figure 25. First Experiment
A 3-D rendering of Figure 24 is provided to better illustrate the site of preferential nucleation.

In experiment 2, a faceted surface was prepared in the same manner as explained for experiment 1. After the presence of faceting was confirmed through LEED, the surface was dosed with 3.0 +/- 0.2 ML of cobalt in one dosing. The surface was then annealed to a temperature of approximately 800K for 3 minutes. Figure 26, below, illustrates the nanoclusters formed using these experimental conditions. The nanoclusters

in this STM image have a more elongated shape and are bigger than the nanocluster from experiment 1.
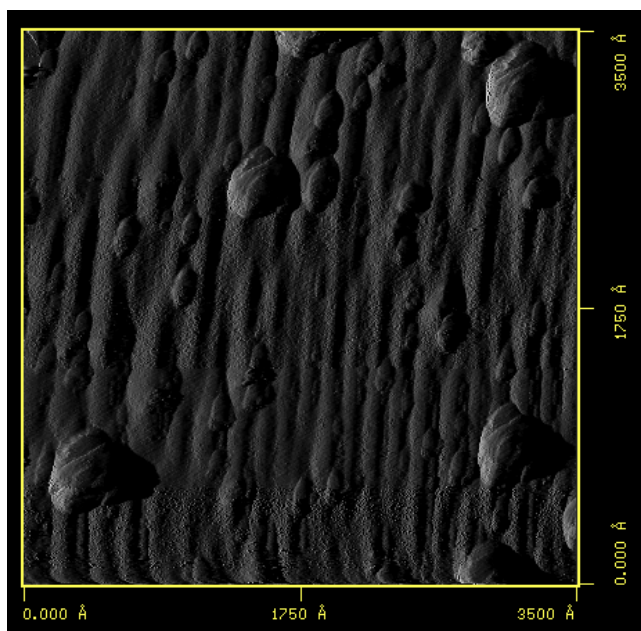

Figure 26. Second Experiment

An elongation of the nanoclusters is visible in this 3500 Å x 3500 Å x-slope STM image from the second experiment.

6.3.1 Controlling Cluster Size

The parameters changed in an attempt to control cluster size were: facet width, cobalt coverage, and annealing temperature. By reducing the facet width, the width of the nanoclusters was reduced as well. Decreasing the cobalt coverage reduced the volume of the nanoclusters. The annealing temperature was reduced by necessity. The previous successful temperature of 800K, used at greater cobalt coverage, effectively destroyed the surface facets. It was decided that by reducing the energy introduced into the system by annealing, the cobalt mobility would be reduced and subsequently, the facets would remain and cobalt nanoclusters would form.

In experiments 3 and 4, the surface was thoroughly cleaned before the faceted surface was prepared. A faceted O/Re($12\bar{3}1$) surface was again created, but this time the parameters were varied slightly to diminish the width of the facets. The procedure of e-beam heating was followed, however, approximately 24L (1 x10^{-7} Torr for 4 min) of oxygen was dosed by backfilling the chamber and monitoring the change in pressure through the use of a Bayard-Alpert ionization gauge. During the dosing process, the surface was e-beam heated three times for approximately 10 seconds each time to a temperature greater than 2200K. Cooling in oxygen created a faceted surface with two facets, ($01\bar{1}0$) and ($11\bar{2}1$). The average width of the facets was approximately 10nm and the facet average height was approximately 2nm.

The surface was then further dosed with another 10L of oxygen causing oxygen saturation. An AES measurement was taken to confirm oxygen surface saturation, followed by a LEED measurement to confirm the surface was properly faceted. The next step was to dose the cobalt, but for about half the time. This provided 1.6 +/- 0.2 ML coverage of cobalt on the surface. AES and LEED measurements were performed again to confirm the cobalt coverage and faceting. Finally, the Co/O/Re($12\bar{3}1$) faceted surface was gently annealed to a temperature less than 680K +/- 30K for 3 minutes. Using these conditions, the size of the cobalt clusters varied. This experiment was performed twice, experiments 3 and 4, to confirm that the results were accurate and reproducible.
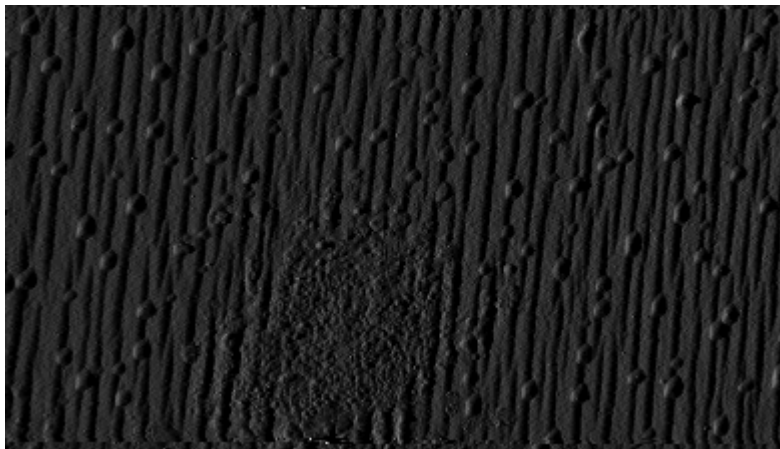
Figure 27. Third Experiment

This 2000 Å x 3500 Å x-slope STM image shows a reduction in facet size as well as cluster size in comparison to Figures 24 and 26. The large formation in the center of the image is anomalous to the surface.

The third experiment's (experiment 3), facet size is approximately 19 Å in height and 95 Å in width. From the image above, Figure 27, it is clear that the facets are smaller in width than those of experiment 1 and 2; also the Co clusters also decrease in size. It is clear from the x-slope of the STM image, Figure 27, that nanoclusters preferentially nucleate in the trenches of the $(01\bar{1}0)$ and $(11\bar{2}1)$ facets. Again, using scan line analysis (see section 6.4, below) it was confirmed that the clusters remain between the facets.

The facet size from the fourth experiment is approximately 20 Å in height and 91 Å in width. From the image below, Figure 28, it is clear that the Co clusters have decreased in size, but increased in density. It is also clear from the x-slope STM image below that nanoclusters preferentially nucleate in the trenches of the $(01\bar{1}0)$ and $(11\bar{2}1)$ facets. Again, using scan line analysis, it was confirmed that the clusters remain between

the facets. Statistical analysis of the nanoclusters for all experiments is provided in the
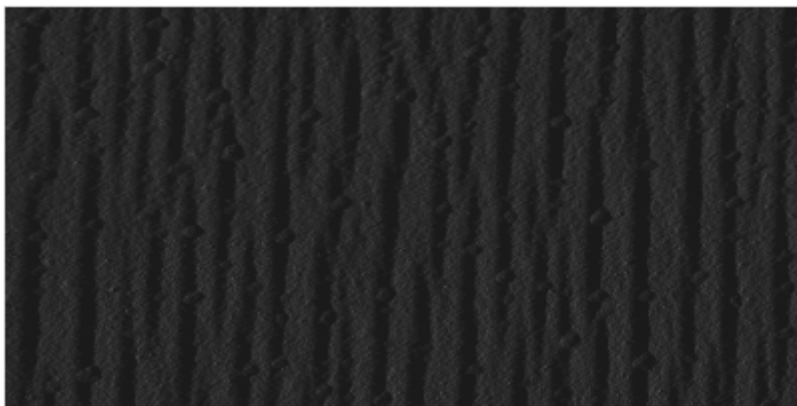
following section.

Figure 28. Fourth Experiment
This 1000 Å x 2000 Å x-slope STM image shows a reduction in facet
size as well as cluster size in comparison to Figures 24, 26, and 27.

6.4 Discussion of Cluster Size Statistics

The general results for this series of experiments are provided in Table 3. The

results will be explained in greater detail in the following paragraphs. However, the

overall trends are clear from the table below.

Exp. #	Co Coverage	Annealing Temp	Facet Width	Cluster Length	Cluster Width	Cluster Height
1	3 +/- 0.4 ML*	T= 800K	~20 nm	16 nm	8.4 nm	20.0 Å
2	3 +/- 0.2 ML	T= 800K	~20 nm	25.9 nm	10.8 nm	34.0 Å
3	1.6 +/- 0.2 ML	T< 680 K	~10 nm	7.1 nm	6.8 nm	25.0 Å
4	1.6 +/- 0.2 ML	T< 680 K	~10 nm	3.0 nm	3.8 nm	17.0 Å

Exp. #	Cluster Density	Cluster Volume
1	808 /μm^2	85 nm^3
2	490 /μm^2	500 nm^3
3	1240 /μm^2	38 nm^3
4	4000 /μm^2	8.2 nm^3

Table 3. This table summarizes the experimental conditions used to make and vary cluster size and density. *Two sequential dosings of cobalt were performed.

For the remainder of this paper the terms cluster length, cluster width, and cluster height will be defined as per the picture below. The cluster height is illustrated by the color in the STM image. The scan line technique is used to determine the height of the clusters accurately, as shown in Figure 29. It is important to note that anomalously large clusters and small clusters were not factored into the following statistics.
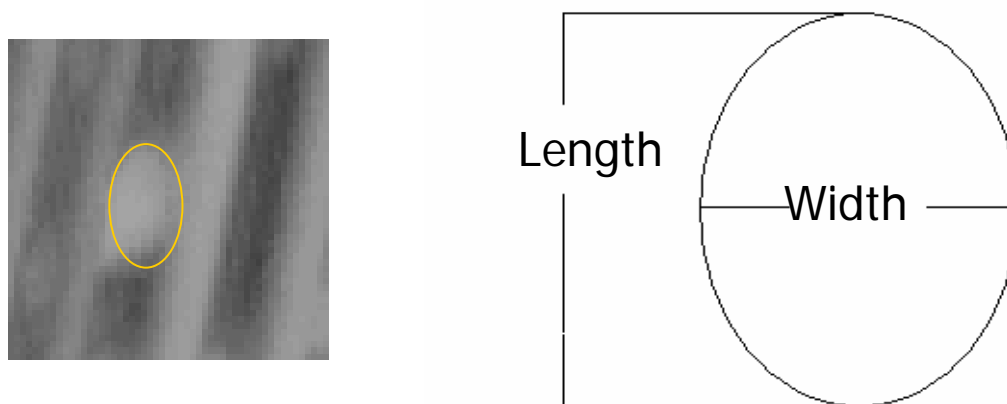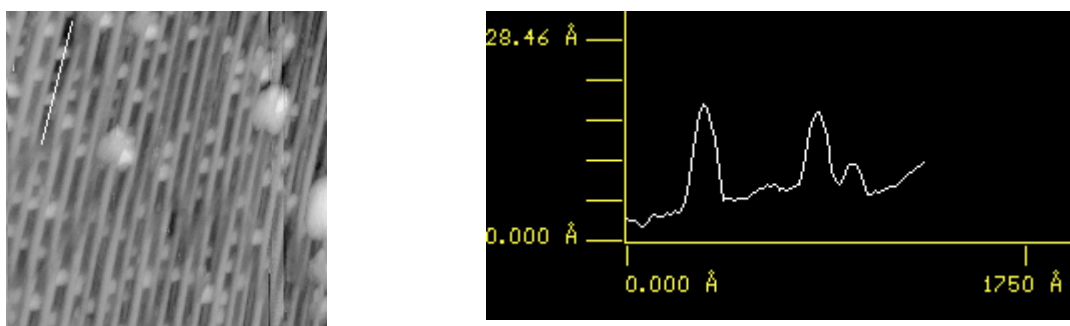

Figure 29. The cluster length and width are defined in the elliptical image above. To determine the approximate height of surface features the scan line technique, provided in the STM software, is used.
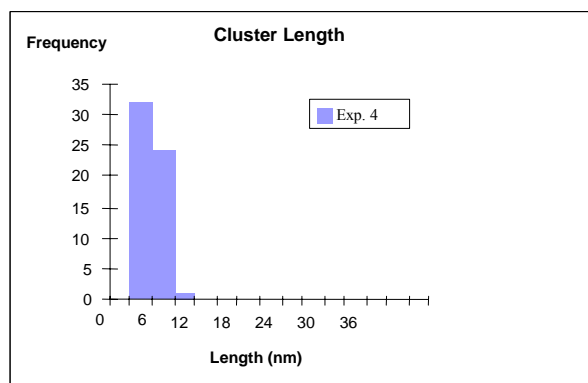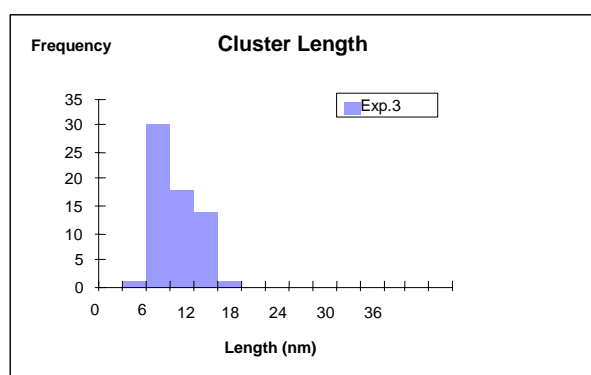

Figure 29. The cluster length and width are defined in the elliptical image above. To determine the approximate height of surface features the scan line technique, provided in the STM software, is used.
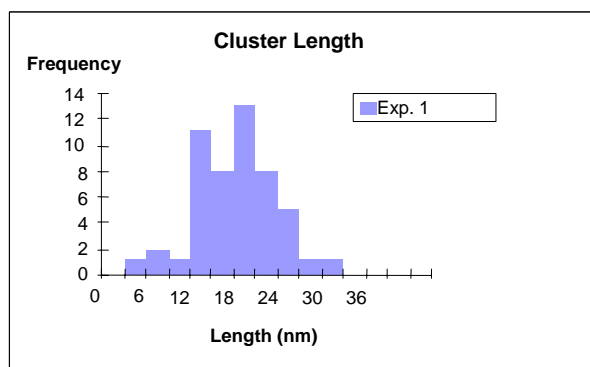
Cluster Length Distribution

Mean Cluster Length L= 3.0 +/- 1.2 nm
Co ~ 1.6 ML, Anneal T<680 K

Mean Cluster Length L= 7.1 +/- 1.2 nm
Co ~ 1.6ML, Anneal T<680 K

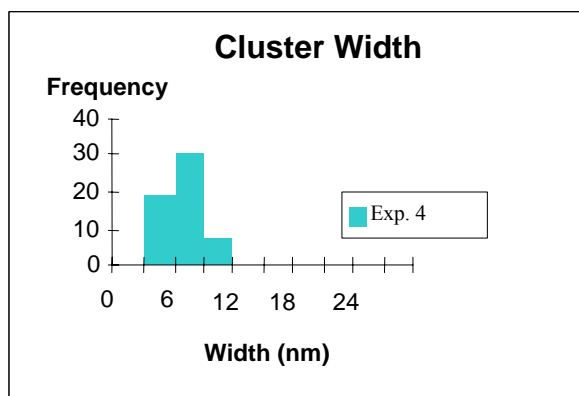Mean Cluster Length L= 16.0 +/- 1.2 nm
Co ~ 3ML, Anneal T~800K
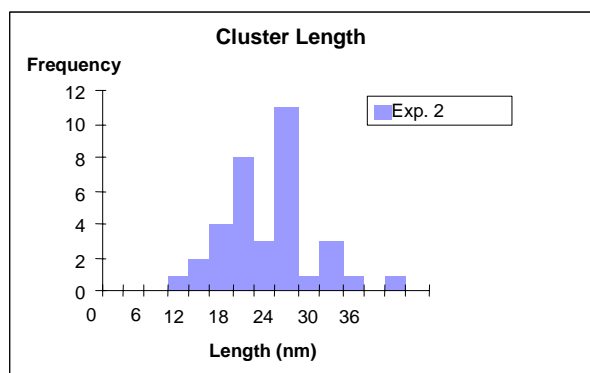
Mean Cluster Length L= 25.9 +/- 1.2 nm
Co ~ 3ML, Anneal T~800K

Table 4. Cluster Length Distribution

Cluster Width Distributions

Cluster Width

Frequency

Mean Cluster Width W= 3.8 +/- 1.2 nm
Co ~ 1.6 ML, Facet W~9.1 nm

Cluster Width

Frequency
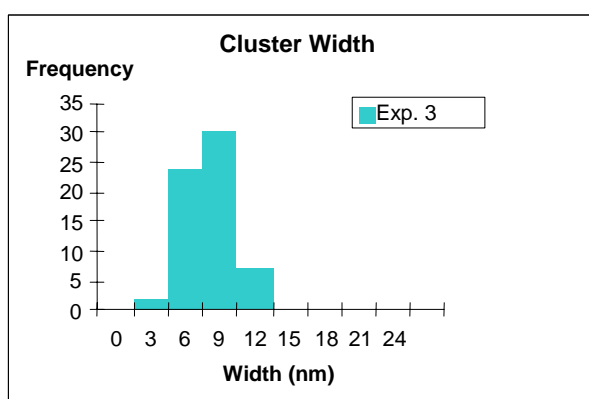
Mean Cluster Width W= 6.8 +/- 1.2 nm
Co ~ 1.6 ML, Facet W~9.5 nm

Cluster Width

Frequency
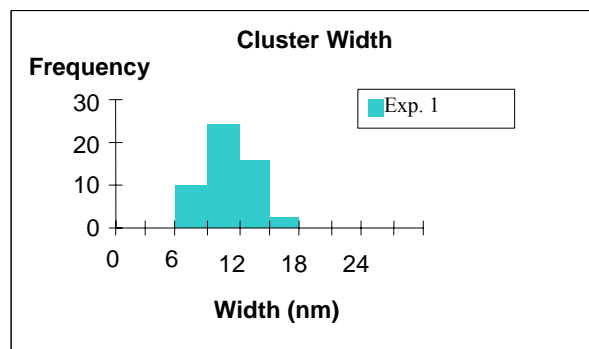
Mean Cluster Width W= 8.4+/- 1.2 nm
Co ~ 3ML, Facet W~20 nm

Cluster Width

Frequency
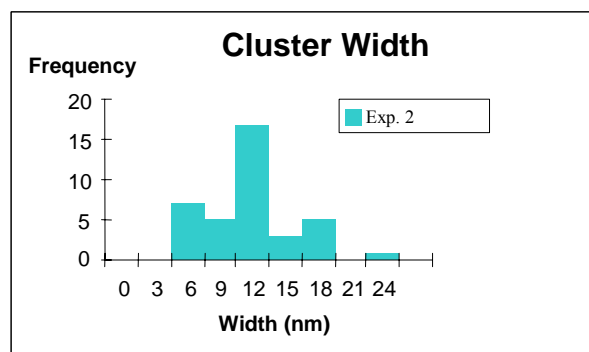
Mean Cluster Width W= 10.8 +/- 1.2 nm
Co ~ 3ML, Facet W~20 nm

Table 5. Cluster Width Distribution

Cluster Height Distributions
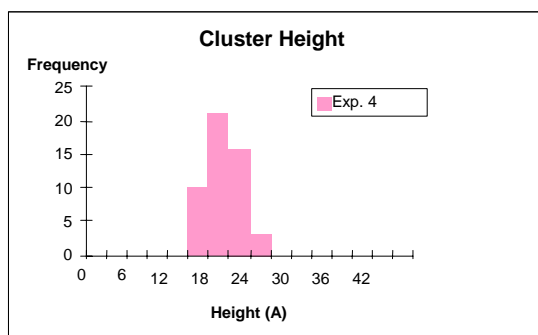
Mean Cluster Height H=17.0 +/- 2.0 Å
Co ~ 1.6 ML, Facet H~15 Å

Mean Cluster Height H=25.0 +/- 2.0 Å
Co ~ 1.6ML, Facet H~15 Å
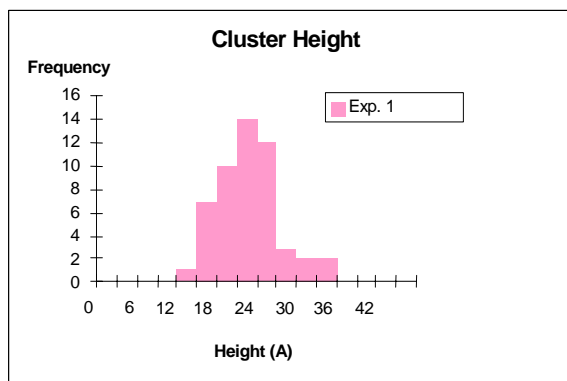
Mean Cluster Height H=20.0 +/- 2.0 Å
Co ~ 3 ML, Facet H~28 Å
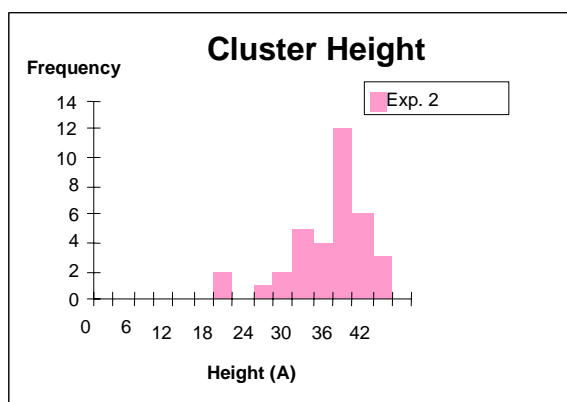
Mean Cluster Height H=34.4 +/- 2.0 Å
Co ~ 3ML, Facet H~28 Å

Table 5. Cluster Height Distribution

The cluster length varied from experiment 1 to experiment 2. The mean length for experiment 1 is 16.0 +/- 1.2 nm and for experiment 2 is 25.9 +/- 1.2 nm. From STM images, it is clear that the clusters in experiment 2 are elongated.

Both experiments 1 and 2 showed similar mean cluster widths. Experiment 1's mean cluster width is 8.4 +/- 1.2 nm, while experiment 2's mean cluster width is 10.8 +/- 1.2 nm. This means that in both cases, the nanoclusters are contained between the facets.

The cluster height varies significantly between the experiments 1 and 2. Experiment 1's mean height is 20.0 +/- 2.0 Å, while the mean height is 34.0 +/- 2.0 Å for experiment 2. This means that experiment 1's mean height is less than the facet height, while the mean cluster height is taller than the facets in experiment 2.

The cluster density may shed some light on the variations between the cluster length, width, and height between experiments 1 and 2. In experiment 1, the cluster density calculated as the number of clusters per surface area is 808 /μm^2. Experiment 2's cluster density is 490 /μm^2. This means that experiment 1's density is almost 1.7 times greater than the second experimental cluster density.

Since the clusters are elongated, it made sense to estimate the cluster volume as ellipsoidal instead of spherical. Taking the mean values as the ellipsoidal axis parameters, the cluster volumes can be approximated in nanometers. Using a hard sphere model, the number of atoms in a cluster can be determined. It is assumed that approximately 60 percent of the calculated ellipsoidal volume corresponds to the actual nanocluster volume; this compensates for partial "wetting" of the faceted substrate by the nanoclusters. The approximate cluster volume from experiment 1 is 85 nm^3 or 1.0x10^4 atoms, while the approximate cluster volume from experiment 2 is 300 nm^3 or 3.7x10^4

atoms. This means that the cluster volume from the second experiment is 3.6 times the size of the first experiment.

The third experiment in which facet size, cobalt coverage, and annealing temperature were all decreased provided interesting cluster statistics. The mean cluster length is approximately 7.1 +/- 1.2 nm, the mean cluster width is approximately 6.8 +/- 1.2 nm, and the mean cluster height is approximately 25.0 +/- 2.0 Å. The cluster width and cluster length decrease with respect to the initial experiment performed. The clusters are still contained between the two facets. Again, the mean cluster height is taller than the facet height (approximately 15 Å).

Again the clusters are slightly elongated, so the cluster volume is calculated based on an ellipsoidal volume. Taking the mean values as the ellipsoidal axis parameters, the cluster volumes can be approximated in cubic nanometers. Using a hard sphere model, the number of atoms in a cluster can be determined. The approximate cluster volume from the first experiment is 38 nm^3 or 4.6×10^3 atoms. This means that the cluster volume from the first experiment (85 nm^3) is 2.2 times the size of the third experiment and the second experiment (300 nm^3) cluster volume is 7.9 times the size of the third experiment. The cluster density from the third experiment is approximately 1240 /μm^2. This means the third experiment has a cluster density 1.5 times the size of the first experiment (808 /μm^2) and is 2.5 times the size of experiment 2 (490 /μm^2).

The fourth experiment, performed to verify the results of experiment 3, shows different results despite keeping the parameters for facet size, cobalt coverage, and annealing temperature approximately the same. The cluster size and density varies significantly from the third experiment. The mean cluster length is approximately 3.0

+/- 1.2 nm, the mean cluster width is approximately 3.8 +/- 1.2 nm, and the mean cluster

height is approximately 17.0 +/- 2.0 Å. The cluster width, length, and height decreased

with respect to the initial experiment performed and the third experiment. However, the

clusters are still contained between the two facets. This time the mean cluster height is

on the order of the facet height (approximately 15 Å). The average cluster volume

decreased significantly to approximately 8.2 nm^3 or 1.0×10^3 atoms. The density of the

clusters increased significantly to 4000 /μm^2, about 3.2 times the density of the third

experiment (1240 /μm^2).

A simplified calculation was carried out to determine the approximate percentage

of the total cobalt in the nanoclusters. Again, the cluster volume was defined by an

ellipsoid of revolution, with axial parameters defined by the mean values of the

histograms above. It is assumed that approximately 60 percent of the calculated

ellipsoidal volume corresponds to the actual nanocluster volume; this compensates for

partial "wetting" of the faceted substrate by the nanoclusters.

Exp.	Co Coverage	Co contained in the nanoclusters
1	3ML*	0.8 ML
2	3ML	1.8 ML
3	1.6 ML	0.6 ML
4	1.6 ML	0.4ML

* 2 sequential dosings of Co were performed

Table 7. Estimate of total Co within the nanoclusters.

From the values in Table 7, it becomes clearer that Stranski-Krastanov growth is

most likely occurring after annealing process. With regards to the first two experiments,

approximately 1ML of the total Co is contained within the nanoclusters. This means

about 2ML of Co remain on the surface in addition to that contained in the nanoclusters.

The third and fourth experiments show that less than 1ML of cobalt is contained within

the nanoclusters, which means that there also is additional cobalt on the faceted surface, approximately 1ML.

A summary of the results discussed in this section can be found in Table 3. From the data provided, it is clear that the clusters formed in all experiments preferentially nucleate in the trenches of the faceted surface. There are a myriad of reasons why the cobalt nanoclusters preferentially nucleate in the trenches of the faceted rhenium surface. For example, there may be an energetic favorability with the atomic geometry at the bottom of the trenches, rather than along either facet or the facet peaks. The reason of preferential nucleation and identifying all of the factors that influence the nanocluster growth are still outstanding challenges and merit more study. However, the general conclusion from these experiments remains, preferential nucleation does occur!

It is also clear that the size of the cobalt nanoclusters diminishes as the facet width, cobalt coverage, and annealing temperature all decreased. While the size of the nanoclusters varies from experiment to experiment, it is clear from the histograms below that for the individual experiments the nanocluster size is relatively uniform. It is currently believed by the catalytic community that a catalyst of uniform nano size may positively influence the catalytic process [25].

Chapter 7

Conclusion

Preferential nucleation of Co nanoclusters was observed on the faceted

O/Re($12\bar{3}1$) surface.   The Co nanoclusters nucleate in the trenches between the ($01\bar{1}0$)

and ($11\bar{2}1$) facets. The Co nanocluster size (length, width, and height) can be controlled

by varying the facet size, cobalt coverage, and annealing temperature. By decreasing the

width of the facets, the nanocluster width decreases. Changing the cobalt coverage

decreases the volume of the nanoclusters. The change in annealing temperature was

necessary to maintain the faceted template on which the nanoclusters nucleate.

Cobalt nanocluster arrays could potentially be used for magnetic-based data

storage. By nucleating nanoclusters which are uniform in size, the selectivity of catalytic

reactions may enhanced[25].   The observation that metallic nanoclusters can be grown

with relatively narrow size distribution by a self-assembly technique, vapor deposition

onto a nanofaceted oxidized substrate, may have broad implications in science and

technology and merits further studies.

References

[1] Bonzel, H. P. and M. Nowicki, Phys. Rev. B 70, 245430 (2004).

[2] *Cobalt.* Los Alamos National Labs Chemistry Division. September 14, 2007 <http://periodic.lanl.gov/elements/27.html>.

[3] Davis, L.E., et. al. *Handbook of Auger Electron Spectroscopy*. (Physical Electronics Industries, Inc., Eden Prairie, MN, 1976).

[4] Drechsler, M. and A. Müller, J. Cryst. Growth 3/4, 518 (1968).

[5] Ermanoski, I., K. Pelhos, W. Chen, J. S. Quinton, and T. E.Madey, Surf. Sci. 549, 1 (2004).

[6] *Faster Nanowires May Advance Nanotechnological Applications For Detecting Glucose, Hormones Or DNA*. Science Direct. September 14, 2007 <http://www.sciencedaily.com/releases/2001/03/010316073033.htm>.

[7] Gambardella, P. et al. Co growth on Pt(997):from monatomic chains to monolayer completion. Surface Science 449, 93-103(2000).

[8] Gambardella, P.; Dallmeyer, A.; Malti, K.; Malagoil, M. C.; Eberhardt, W.; Kem, K.; Carbone, C. *Ferromagnetism in one-dimensional monatomic metal chains.* Nature (London, United Kingdom) (2002), 416(6878), 301-304.

[9] Glaspell, Garry; Abdelsayed, Victor; Saoud, Khaled M.; El-Shall, M. Samy. *Vapor -phase synthesis of metallic and intermetallic nanoparticles and nanowires : magnetic and catalytic properties.* Pure and Applied Chemistry (2006), 78(9), 1667-1689.

[10] Gray, D. E., *American Institute of Physics Handbook*, 3rd ed. (McGraw-Hill, New York, 1972).

[11] Herring C., Phys. Rev. 82, 87 (1951).

[12] Kittel, Charles. *Introduction to Solid State Physics.* (John Wiley and Sons, Inc., New York, 2004).

[13] Kumar, R. and H. E. Grenga, Surf. Sci. 50, 399 (1975).

[14] Madey, T. E., C.-H. Nien, K. Pelhos, J. J. Kolodziej, I. M. Abdelrehim,and H.-S. Tao, Surf. Sci. 438, 191(1999).

[15] Madey, T. E., J. Guan, C.-H. Nien, H.-S. Tao, C.-Z. Dong, and R.A. Campbell, Surf. Rev. Lett. **3**, 1315 (1996).

[16] Mattox, D.M. *Handbook of Physical Vapor Deposition (PVD) Processing* (William Andrew Publishing/Noyes, Park Ridge, NJ,1998).

[17] Morgenstern, Karina; Kibsgaard, Jakob; Lauritsen, Jeppe V.; Laegsgaard, Erik; Besenbacher, Flemming. *Cobalt growth on two related close-packed noble metal surfaces.* Surface Science (2007), 601(9), 1967-1972.

[18] Nien, C.-H. and T. E. Madey, Surf. Sci. 380, L52 (1996).

[19] *Nucleation in Metals and Alloys.* Andrew Green and Phil Pranghill. Version 2.1. September 14, 2007 < http://www.matter.org.uk/matscicdrom/manual/nu.html>.

[20] The Process of Electrochemical Deposition. Manuel DaSilva. Purdue University. September 14, 2007 <http://cobweb.ecn.purdue.edu/~mdasilva/Electrodeposition.shtml >.

[21] Overbury, S. H., P. A. Bertrand, and G. A. Somorjai, Chem. Rev. (Washington, D.C.) 75, 547 (1975).

[22] *Rhenium.* Los Alamos National Labs Chemistry Division. September 14, 2007 <http://periodic.lanl.gov/elements/75.html>.

[23]   Roeder, Holger; Hahn, Elmar; Brune, Harald; Bucher, Jean Pierre; Kern, Klaus. *Building one - and two - dimensional nanostructures by diffusion - controlled aggregation at surfaces.* Nature (London, United Kingdom) (1993), 366(6451), 141-3.

[24]   Spence, M. J. S., A. Hung, I. K. Snook, and I. Yarovsky, Surf. Sci. 513, 389 (2002).

[25]   Somorjai, G.A. and Y.G. Borodko, *Catal. Lett*. 76 (2001) 1.

[26]   *Suspended Gold Nanowires.* Takayanagi, Kunio. September 14, 2007 <http://www.jsapi.jsap.or.jp/Pdf/Number03/CuttingEdge1.pdf>.

[27]   Vitos, L., A. V. Ruban, H. L. Skriver, and J. Kollar, Surf. Sci. 411, 186 (1998) and reference therein.

[28]   Wang, Hao; Chen, Wenhua; Madey, Theodore E. *Morphological evolution in oxygen - induced faceting of Re(12-31).* Physical Review B: Condensed Matter and Materials Physics (2006), 74(20).

[29]   Woodruff, D. F. and T.A. Delchar, *Modern Techniques of Surface Science-second edition.* (Cambridge University Press, Cambridge, 1994).

[30]   Yates Jr, J.T. *Experimental innovations in surface science: A guide to practical laboratory methods and instruments.* (Springer-Verlag, New York, 1998).

[31]   Yu D. and M. Scheffler, Phys. Rev. B 70, 155417 (2004).

[32]   Zangwill, A. *Physics at Surfaces.* (Cambridge University Press, Cambridge, (1988).

Appendix

A.1 Future Experiments

There are a myriad of experiments that can be performed to enhance the understanding of the cobalt nanoclusters. An experiment can be performed by varying the width of facet ridges; in this case further information on nanoclusters' widths can be determined. Another experiment can be carried out by varying the sample annealing temperature after the deposition of Co or by depositing Co onto heated substrate; in this case, the mobility of the Co atoms will change and perhaps the nanoclusters will change as well. Further experimentation can be done by changing the oxygen pre-coverage on the Re facets before the deposition of Co; in this case, the surface could potentially have a completely different morphology. By varying coverage of the Co deposited in a future experiment, the cluster size, volume, and density could change dramatically. An additional experiment can be performed by depositing Co onto more extensively faceted Re; in this case new nanostructures may be visible. A different experiment can be executed by depositing different metals, with varying mismatch parameters, to discover different nanostructures.

A.2 Useful Self-written Programs

2.1 Auger Electron Spectroscopy Program

After encountering the problem of being unable to open the AES data in Excel, this program was written to fix the problem. As reminder for users not familiar with the Rutgers physics department Linux OS computers, to compile a program the command

line must read > g++ -o getrid_v getrid_v.cpp, to run the program the command line must

read > ./getrid_v .

```
Getrid_V.cpp
// This program is used to update the old Perkin-Elmer Auger files so
// the file is compatible with modern computer systems
#include <iostream>
#include <fstream>
#include <cstdlib>
#include <string>
using namespace std;

int main()
{
  string s;
  string filename;
  ifstream input;  // input stream
  cout << "input file name: " << endl;
  cin >> filename;
  input.open(filename.c_str());  //open stream
  ofstream output; //output stream
  output.open("results.dat");   // change results.dat or overwritten
  if(input.fail())  //bad file case
    { cout << "failed input file" << endl;
    exit(1);
    }
  while(getline(input,s, '\n'))  // until eof
    {
      if(s[0] != 'V')  // first char in string=V
      {
        output << s << endl;
      }
      }
  input.close();  //close input file

  output.close();  //close output file

  return 0;
}
```

2.2   Scanning Tunneling Microscopy Program

The McAllister STM software provided with the equipment does not render STM

images in a format that is understood by Windows XP or Unix Image processing

programs. In order to look at the STM images, a computer running DOS or Windows 95

must be used. This program was written in an attempt to open STM images on modern

computers so analysis of the images would be faster. Upon completion of this program, a

more versatile free software, "Scanning Probe Image Processor," was discovered that

both converted the file format and provided many tools to make analysis easier.

```cpp
// The purpose of this program is to update the old .STM file to a new
// .PGM file for conversion and then use in a modern imaging software
//  program.
#include <iostream>
#include <fstream>
#include <cstdlib>
#include <string>

using namespace std;

int main()
{
      string s;
      int length;
      char * buffer;
      string filename;

      ifstream input;  // input stream
      input.open("04170609.STM");  //open stream

      ofstream output; //output stream
      output.open("convert.pgm");    // change results.dat or
overwritten
      ofstream datput;
      datput.open("stm2int1.dat");  //binary to int data in row form
      if(input.fail())  //bad file case
    { cout << "failed input file" << endl;
            exit(1);
    }

      output<< "P5"<< " " << 400 << " " << 400 << endl;
      output << 255 << endl;

      //get length of file
      input.seekg (0, ios::end);
      length = input.tellg();
      input.seekg (0,ios::beg);

      // allocate memory:
      buffer = new char [length];
      int data_offset = 780;

      //read data as a block
      input.read( buffer,length);

      float max_max =0;

      for(int i=data_offset; i<length; i=i+2 )
      {
        datput << (int) buffer[i] <<" " << (int) buffer[i+1] << endl;
            int number = abs(buffer[i]) + 128;
          int exponent = buffer[i+1]*255+number;
```

```
            if ( exponent > max_max)
            {
                    max_max = exponent;
            }
            // if((int) buffer[i]<0 )   cout << (int) buffer[i] <<
endl;
             //output << number;
      }


      char curr_Value;
      float scaled_Value;

      for(int i=data_offset; i<length; i=i+2 )
      {
            float number = abs(buffer[i]) + 128;
            float exponent = buffer[i+1]*255+number;

            scaled_Value = (exponent/max_max)*255.0;
            curr_Value = scaled_Value;

                  if(scaled_Value >255) cout << scaled_Value <<endl;
            output<< curr_Value;
      }


      input.close();  //close input file
      output.close();  //close output file
      datput.close();
      return 0;
}
```